1151

TRANSPORTATION RESEARCH RECORD

Hydraulic Erosion

TRANSPORTATION RESEARCH BOARD
NATIONAL RESEARCH COUNCIL
WASHINGTON, D.C. 1987

Transportation Research Record 1151
Price: $6.50
Editor: Elizabeth W. Kaplan
Typesetting and layout: Betty L. Hawkins

modes
1 highway transportation
3 rail transportation

subject area
22 hydrology and hydraulics

Transportation Research Board publications are available by ordering directly from TRB. They may also be obtained on a regular basis through organizational or individual affiliation with TRB; affiliates or library subscribers are eligible for substantial discounts. For further information, write to the Transportation Research Board, National Research Council, 2101 Constitution Avenue, N.W., Washington, D.C. 20418.

Printed in the United States of America

Library of Congress Cataloging-In-Publication Data
National Research Council. Transportation Research Board.

Hydraulic erosion.
p. cm. — (Transportation research record, ISSN 0361-1981 ; 1151)
ISBN 0-309-04655-6
1. Roads—Embankments. 2. Roads—Design. 3. Soil erosion.
I. National Research Council (U.S.). Transportation Research Board.
II. Series.
TE7.H5 no. 1151
[TE210.8]
380.5 s—dc 19
[625.7'34] 88–17995
CIP

Sponsorship of Transportation Research Record 1151

GROUP 2—DESIGN AND CONSTRUCTION OF TRANSPORTATION FACILITIES

General Design Section
Jarvis D. Michie, Dynatech Engineering, Inc., chairman

Committee on Hydrology, Hydraulics and Water Quality
J. Sterling Jones, Federal Highway Administration, chairman
James E. Alleman, Frank X. Browne, Howard H. Chang, Darwin L. Christensen, Stanley R. Davis, David J. Flavell, Thomas L. Hart, Carl M. Hirsch, Richard B. Howell, Kenneth D. Kerri, Floyd J. Laumann, Byron Nelson Lord, Walter F. Megahan, Don L. Potter, Robert E. Rallison, Brian M. Reich, J. Reichert, Everett V. Richardson, Verne R. Scheider, Robert F. Shattuck, Michael D. Smith, Charles Whittle, Ken Young, Michael E. Zeller

George W. Ring III, Transportation Research Board staff

The organizational units, officers, and members are as of December 31, 1986

Transportation Research Record 1151

The **Transportation Research Record** series consists of collections of papers on a given subject. Most of the papers in a Transportation Research Record were originally prepared for presentation at a TRB Annual Meeting. All papers (both Annual Meeting papers and those submitted solely for publication) have been reviewed and accepted for publication by TRB's peer review process according to procedures approved by a Report Review Committee consisting of members of the National Academy of Sciences, the National Academy of Engineering, and the Institute of Medicine.

The views expressed in these papers are those of the authors and do not necessarily reflect those of the sponsoring committee, the Transportation Research Board, the National Research Council, or the sponsors of TRB activities.

Transportation Research Records are issued irregularly; approximately 50 are released each year. Each is classified according to the modes and subject areas dealt with in the individual papers it contains. TRB publications are available on direct order from TRB, or they may be obtained on a regular basis through organizational or individual affiliation with TRB. Affiliates or library subscribers are eligible for substantial discounts. For further information, write to the Transportation Research Board, National Research Council, 2101 Constitution Avenue, N.W., Washington, D.C. 20418.

Contents

Foreword

The four papers in this Record all deal with some form of, or the control of, erosion by water.

Chen and Anderson evaluate the effectiveness of gabion mattresses, soil cement, geowebs, enkamat, and vegetation in protecting soil embankments subject to overtopping. Computer simulation and laboratory tests indicate that each material affords protection, but some are effective only at low velocities associated with low overtopping depths.

Simon and Hupp developed a computer program that models streambed degradation and aggradation of channels approaching a new equilibrium after man-made modifications to alluvial channels. The program is based on streambed degradation and aggradation measurement in the Obion, Forked Deer, and Hatchie river basins in western Tennessee and includes a six-stage process of bank slope development.

Simon, Sarikelle, and Korom present a model study of ring chamber design for dissipation of energy in culverts that operate under inlet control on steep slopes. Velocity reductions versus inlet Froude numbers are given for prototype culverts.

Laboratory studies of erosion rates of compacted, unsaturated, montmorillonite clay as a function of sodium (salt) absorption ratio (SAR) and tractive stress are presented by Shaikh, Ruff, and Abt. The erosion rate coefficient was decreased by two orders of magnitude when the SAR was increased from 0.4 to 11.

Methodology for Estimating Embankment Damage Caused by Flood Overtopping

YUNG-HAI CHEN AND BRADLEY A. ANDERSON

An investigation of the erosion of highway embankments caused by flood overtopping is presented. Data collected from a series of laboratory tests and field investigations were evaluated to develop a methodology for quantitatively determining embankment damage. A computer model, verified by using laboratory and field data, was developed to simulate the hydraulics of overtopping flow and to estimate the erosion rate of the embankment. The computer model was used to generate nomographs and to develop a step-by-step procedure for estimating damage to roadway embankments. The effectiveness of five embankment protection measures was evaluated during the laboratory tests. Critical velocities and failure criteria associated with each protective measure were qualitatively established.

Estimating embankment damage caused by flood overtopping is a relatively new issue for highway engineers. Traditionally, the consequences of floods larger than the "design flood" have been ignored. Although there have been several attempts to develop an approximate method of estimating embankment damage, all attempts lacked the benefit of a set of controlled experimental data and differed by several orders of magnitude.

Numerous materials have been used for protecting embankments from flood erosion. These measures reduce embankment erosion by (*a*) protecting or strengthening the soil to increase its resistance to erosion and (*b*) increasing surface roughness to reduce the erosive force of the flood. Materials commonly used for protection include vegetation, riprap, soil cement, and geotextiles. Information about the performance of the various materials available to protect embankments from damage caused by flood overtopping is quite limited.

The objectives of this project were to review the pertinent literature, collect available field data, and conduct laboratory tests to develop a methodology to quantitatively determine embankment damage. The effectiveness and failure criteria of various types of protection were also evaluated as part of the project. The literature review, field data, and laboratory data were analyzed to develop embankment erosion equations that take into account the configuration and material characteristics of the embankment and the hydraulics of overtopping flow. A mathematical model was developed and verified using the collected field and laboratory data. The model was then used to generate design charts for estimating embankment damage caused by floods of various overtopping depths and tailwater conditions. The major results of that study are presented in this paper.

Simons, Li & Associates, Inc., 3555 Stanford Road, P.O. Box 1816, Fort Collins, Colo. 80522.

LABORATORY EMBANKMENT TEST PROGRAM

Embankment overtopping tests were conducted in an outdoor testing facility at the Engineering Research Center (ERC) of Colorado State University. The outdoor testing facility was designed to conduct tests on full-scale roadway embankments. Use of a testing facility that allows full-scale tests minimized the inaccuracies inherent in modeling the physical processes associated with the hydraulic and sediment transport mechanics of embankment erosion.

During this study soil testing was done to evaluate all fill material used in construction of the embankment test sections. Soil materials were selected in accordance with specifications provided by the FHWA and included a clayey sand mixture (Unified Soil Classification CL), as well as a sandy, more erosive soil (Unified Soil Classification SM-SC). Laboratory and field tests were performed to classify and determine the engineering properties of the fill material. The soil tests, conducted in accordance with ASTM procedures, provided information on soil classification, grain-size distribution, Atterberg limits, hydraulic conductivity, critical shear stress, shear strength, compaction characteristics, and dispersivity. Table 1 gives information on the two soils tested during this investigation.

TABLE 1 SOIL TEST RESULTS

Soil Property and Test	Unified Soil Classification	
	CL	SM-SC
Grain-size distribution		
Percent sand	40	59
Percent passing No. 200 sieve	60	41
Atterberg limits		
Liquid limit	32.7–35.1	24.4
Plastic limit	19.3–22.3	18.7
Plasticity index	11.7–15.7	5.7
AASHTO classification	A-6	A-4(0)
Compaction		
Optimum moisture content (%)	13–19	14.7
Maximum dry density (lb/ft^3)	102–111	113.5

All embankment test sections were constructed 6 ft high and allowed for a top pavement width of 12 ft and a shoulder width of 10 ft. The side slope of the embankments tested during this study varied from 2:1 (horizontal to vertical) to 3:1. The two soils described previously were used as fill material, and two roadway surfaces (soil and paved) were tested along with five embankment protection measures (grass, geoweb, enkamat,

gabion, and soil cement). The flood overtopping tests included testing a variety of side slopes, overtopping depths, water-surface drops, overtopping durations, road surfaces, and embankment protection measures. The information gained from the bare-soil tests provided a basis for judging the erosion protection afforded by pavement, vegetation, and the other embankment protection measures.

The data collected during each laboratory test included discharge, velocity, overtopping depth, water-surface profile, and embankment profile. The laboratory test data coupled with the field data collected in this study were analyzed to determine the hydraulic conditions associated with embankment overtopping flow. Given the laboratory and field data, the following analyses were specifically conducted:

- The fixed-bed embankment test data were analyzed to determine hydraulic conditions of overtopping flow including flow mode, discharge coefficients, local velocity, and shear stress immediately above the embankment surface. A mathematical model was developed to determine the hydraulic conditions of overtopping flow and was verified using the test data. The results of analysis are presented in the section entitled Hydraulics of Flow Over an Embankment.
- Data collected during the initial laboratory tests were analyzed to (*a*) determine the erosion patterns and critical shear stress of bare soil, (*b*) evaluate applicability of existing soil erosion equations, and (*c*) establish soil erosion equations that can be used to determine the rate of embankment soil erosion as a function of the soil characteristics and the hydraulics of overtopping flow. The results of analysis are presented in the section entitled Parameters and Equations Governing Erosion of Embankment.
- A mathematical model was developed by incorporating the erosion equations into the mathematical model produced for determining the hydraulic conditions of overtopping flow. This model was used to determine the embankment erosion rate due to flood overtopping. The model was calibrated using the results of tests conducted on bare soils. The effects of pavement and grass were assessed by comparing the results of tests with and without pavement and grass. The model was then applied to develop a set of nomographs for estimating embankment damage taking various flood conditions and embankment characteristics into consideration. These nomographs were verified using the field data described in the section entitled Collection of Field Embankment Damage Data. The results of the analysis are presented in Development of a Procedure for Determining Embankment Erosion Caused by Flood Overtopping.
- On the basis of the results of the laboratory tests, the effects of various protective measures on embankment stability were assessed. The critical conditions that would initiate the failure of these protective measures were determined and are discussed in the section entitled Evaluation of Embankment Protection Measures.

COLLECTION OF FIELD EMBANKMENT DAMAGE DATA

The field data collected during this project included data on roadway embankment damage caused by flood overtopping at 21 sites in 5 states. The data were collected by a joint force of personnel from the FHWA; state highway agencies; the U.S. Geological Survey; and Simons, Li & Associates, Inc. (SLA). Data were collected from five sites in Arkansas and three sites in Missouri that were affected by a flood in December 1982, four sites in Wyoming and one site in Colorado that were affected by a May 1983 flood, five sites in Arizona that were affected by a September 1983 flood, and three sites in Wyoming that were affected by a flood in August 1985. Details of field data are presented elsewhere *(1, 2)*. The field data are limited to the flow hydraulics and overtopping conditions at peak flow, total embankment damage after the flood, and minimal soil data (Unified Soil Classification and size distribution). The field data, however, proved useful for verification of the modeling assumptions and the procedure developed for determining embankment erosion.

HYDRAULICS OF FLOW OVER AN EMBANKMENT

Flow Patterns

An understanding of the hydraulics of water flowing over an embankment provides a basis for understanding the erosion process. Various flow patterns have been observed as water flows over an embankment. These flow patterns were classified by Kindsvater *(3)* as free-plunging flow, free surface flow, and submerged flow. Plunging flow occurs when the jet plunges under the tailwater surface, producing a submerged hydraulic jump on the downstream slope. Surface flow occurs when the jet separates from the roadway surface at the downstream shoulder and "rides" over the tailwater surface. Whereas free flow can be either a plunging or a surface flow, submerged flow is always a surface flow. Plunging flow generally causes more embankment erosion than does surface flow.

The free-flow transition range is the range of tailwater levels within which a given discharge can produce either a plunging flow or a surface flow, depending on the antecedent conditions. Thus, if the tailwater is initially low and the flow plunging, this pattern persists as the tailwater level rises until it reaches the upper limit of the transition range, whereupon the plunging flow changes abruptly to a surface flow. However, if the tailwater is initially high and the flow is a surface flow, this pattern persists as the tailwater drops until it reaches the lower limit of the transition range, whereupon the flow pattern changes abruptly to plunging flow. The stability or persistence of the flow patterns within the transition range is related to the inertia of the large, horizontal-axis rollers that occur on the downstream side of the embankment.

Kindsvater *(3)* presented charts for determining flow patterns over embankments. Figure 1 shows the variables used in the charts and Figure 2 shows a summary of the limits of the incipient submergence and free-flow transition ranges for a screen-wire roughness surface. Figure 2 was checked using the data collected from rigid embankment tests and evaluated to determine its applicability to large-scale embankments. The test results are also plotted in Figure 2. These results indicate that Figure 2 is applicable to the determination of the transition range between surface and plunging flow for large-scale embankments.

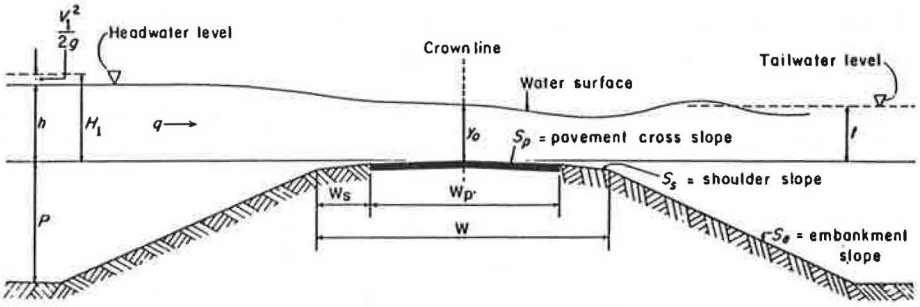

FIGURE 1 Principal variables needed to describe flow over an embankment.

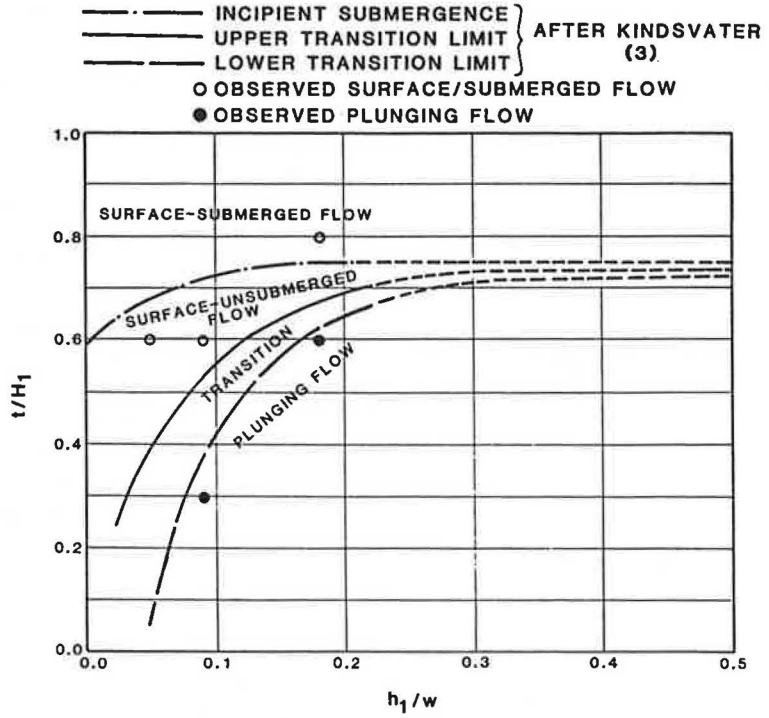

FIGURE 2 Summary of incipient submergence and free-flow transition ranges.

Examination of velocity data reveals that, for surface flow, the velocity over the downstream slope surface would be in reversed direction. Its magnitude would be relatively constant down the slope and generally less than the depth-averaged velocity. Figure 3 shows a typical water-surface and velocity profile for surface flow. Examination of the rigid embankment test data yields

$$V_r = -0.15\ V_u \tag{1}$$

Where V_r is the flow velocity over the downstream slope surface and V_u is the average velocity at the upper edge of the slope.

For plunging flow the velocity over the downstream slope surface would generally be larger than the depth-averaged velocity for the with-tailwater condition and would be the same as the depth-averaged velocity for the free-fall condition. Figure 4 shows typical water-surface and velocity profiles for plunging flow. The following relation was developed for plunging flow with the tailwater condition:

$$V_r = 0.55\ V_{uj} \tag{2}$$

where V_{uj} is the averaged flow velocity immediately upstream of a hydraulic jump.

For plunging flow with no appreciable tailwater, the representative velocity (v_r) would be the average flow velocities along the embankment

$$v_r = v_i \tag{3}$$

where v_i is the average velocity at a point (i) on the embankment.

The local shear stress can be related to local velocity by

$$\tau = {}^1/_8 f \rho\ V_r^2 \tag{4}$$

where

f = the Darcy-Weisbach coefficient,
ρ = the water density, and

V_r = a local reference velocity equal to the depth-averaged velocity over the embankment crest and upstream slope, or equal to that determined from Equation 1 or 2 for the downstream slope.

Discharge Equations for Flow Over an Embankment

The generally accepted form of the equation that computes discharge over an embankment for the free-flow condition is

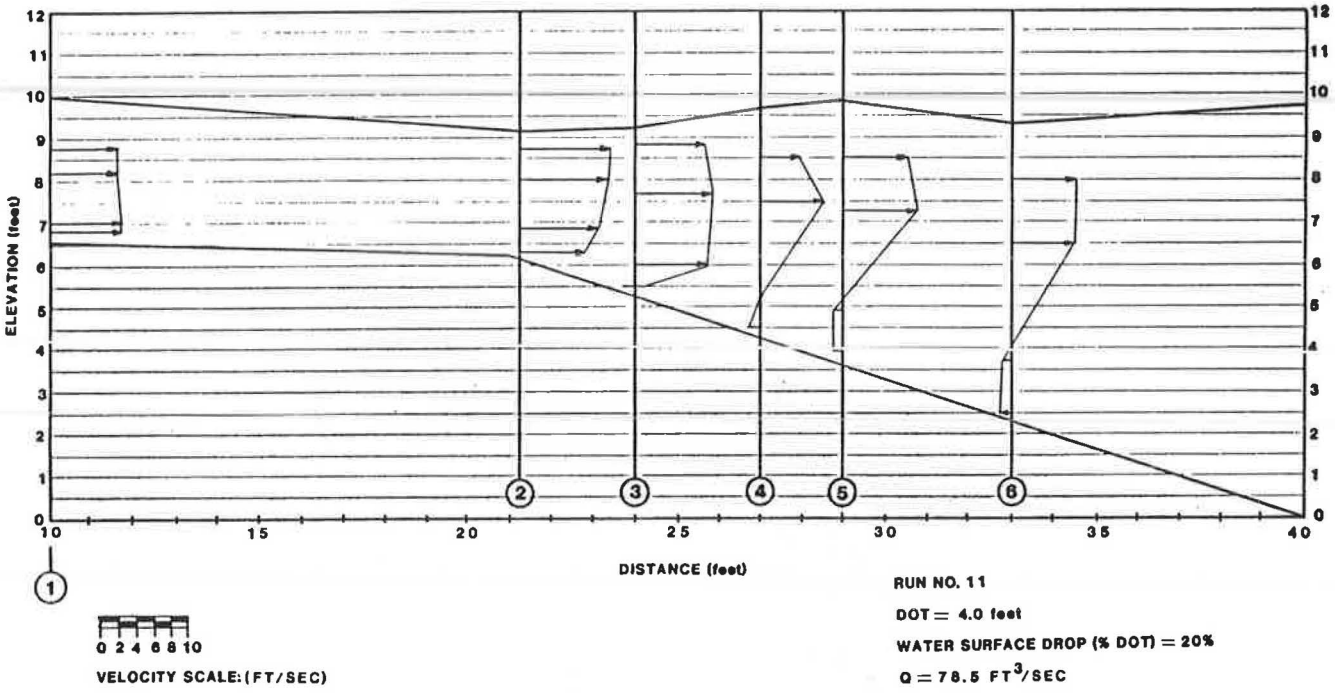

FIGURE 3 Water-surface and velocity profiles for surface flow.

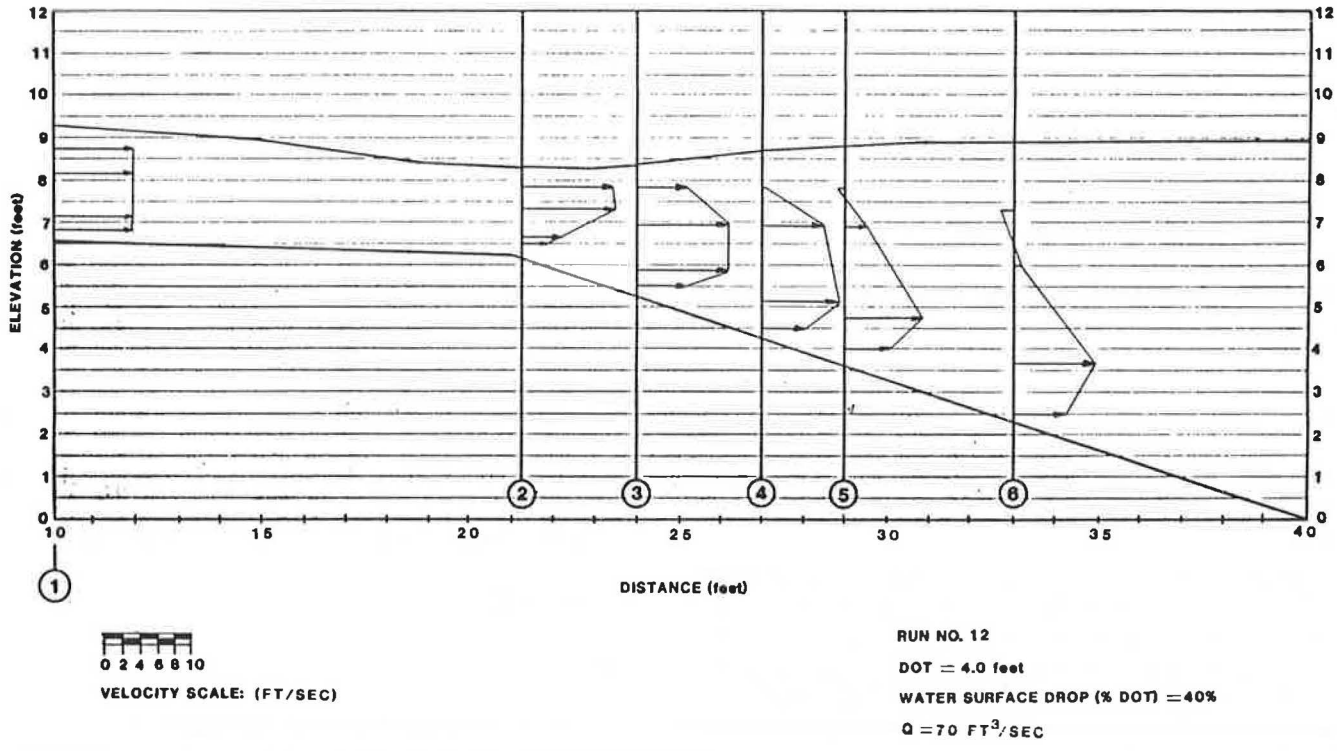

FIGURE 4 Water-surface and velocity profiles for plunging flow.

$$q = C\ H_1^{3/2} \quad (5)$$

where

q = discharge per unit width,
C = a discharge coefficient, and
H_1 = total head above the embankment crest as defined in Figure 1.

Using Kindsvater's data for a smooth roadway surface, Bradley *(4)* presented Figure 5 to determine the discharge coefficient. To determine the discharge flowing over a roadway, first enter Curve B (Figure 5) with H_1/W and obtain the free-flow coefficient of discharge (C). Should the value of H_1/W be less than 0.15, it is suggested that C be read from Curve A of the same figure. If submergence is present (i.e., if t/H_1 is greater than 0.7), enter Curve C with the proper value of submergence in percent and read off the submergence factor (C_s/C). The resulting discharge is obtained by substituting values in the expression

$$Q = C\ L\ H^{3/2}\ (C_s/C) \quad (6)$$

where

L = the length of inundated roadway,
H_1 = the total upstream head measured above the crown of the roadway, and
C and C_s = coefficients of discharge for free flow and submerged flow, respectively.

If the depth of flow varies along the roadway, it is advisable to divide the inundated portion into reaches and compute the discharge over each reach separately. The process, of course, can be reversed to aid in determining backwater for a combination of bridge and roadway configurations.

Experimental results of this study indicated that Figure 5 is applicable to the determination of the coefficient of discharge for flow over full-scale embankments. The effect of embankment side slope on the flow is insignificant except perhaps for the effect on rolling waves on the downstream side. For the free-flow case, variations in embankment height, pavement, cross slope and shoulder slope do not affect the hydraulic conditions of flow on the embankment crest.

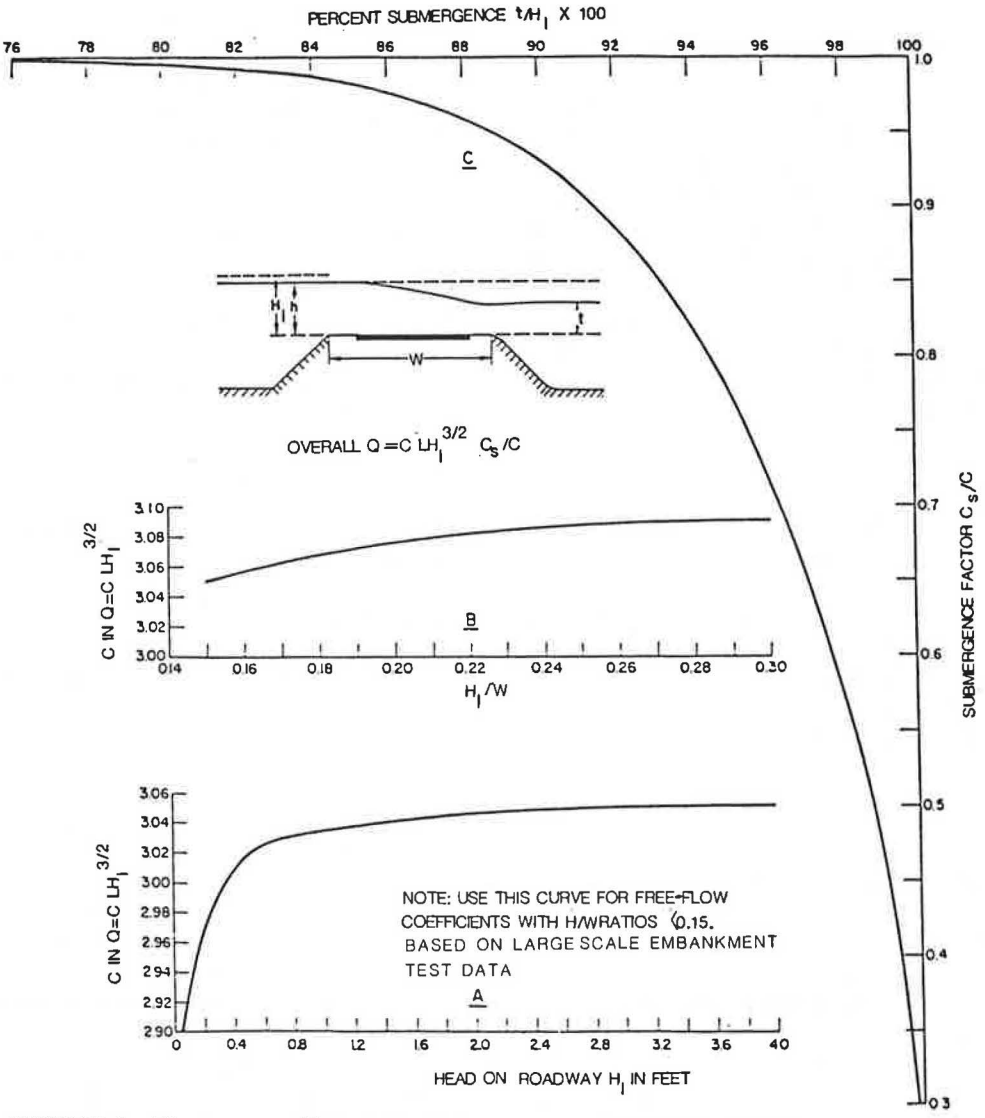

FIGURE 5 Discharge coefficients for flow over roadway embankment *(4)*.

PARAMETERS AND EQUATIONS GOVERNING EROSION OF EMBANKMENT

The erosion of soil, particularly cohesive soil, is complicated because many controlling parameters act interdependently. Principal factors involved are the physical and chemical properties of the soil itself, its behavior when partly and fully saturated, and the hydraulic properties of the flow.

When embankments are overtopped by flood waters, erosion damage can be significant because of high velocities on the downstream side of the embankment. As the shear stress exerted by the flow exceeds the critical shear stress of the soil, erosion begins. Shear stress increases with velocity. Velocity depends on the headwater and tailwater conditions. Another important parameter is the erodibility of the soil. Cohesive soil or soil with larger particles is more resistant to erosion than are noncohesive, fine-grained soils. The duration of overtopping affects the amount of damage.

The critical or permissible shear stress and velocity are defined as the largest shear stress and velocity of flow that will not cause erosion. For noncohesive materials, the following equation can be used to determine the critical shear stress *(5)*:

$$\tau_c = 0.05\ (\gamma_s - \gamma)\ d_{50} \tag{7}$$

where γ_s and γ are the unit weights of soil and water, respectively, and d_{50} is the median particle size of the soil. Equation 7 is valid for a shear Reynolds number greater than 70.

Several relations for determining critical shear stress have been developed for cohesive soil. In the study of hydraulic erosive forces required to initiate motion of cohesive soils in open channels, Smerdon and Beasley *(6, 7)* found that critical tractive force of cohesive soil correlated well with plasticity index. The relation developed for 11 uncompacted Missouri soils, ranging from a silty loam soil with little cohesion to a highly cohesive clay soil, was

$$\tau_c = 0.0034\ (PI)^{0.84} \tag{8}$$

where *PI* is the plasticity index. Because soils used in highway embankments are normally compacted, a new relationship was needed for τ_c.

Because the plasticity index is generally available or can be easily determined for different types of soils, it was decided that a power relation in the form of Equation 8 would be used in this study to determine critical shear stress. By using the data from McWhorter et al. *(8)* and soil data from this study, the following relation was obtained:

$$\tau_c = 0.019\ (PI)^{0.58} \tag{9}$$

McWhorter et al. *(8)* conducted a comprehensive study for the design of open channels using artificial lining materials. In the course of experimentation, 11 soils ranging from a noncohesive sand gravel to an inorganic clay were tested. McWhorter et al. conducted a series of tests to determine erosion rates of these soils by flow. In this study, the erosion rates were plotted versus shear stress for different soils. Regression lines were fit to the data points and then extended to zero erosion to determine the critical shear stress. These data are plotted in Figure 6 and fitted by a power function (Equation 9). The critical shear stress for the clayey sandy soil used in this project is also plotted in Figure 6. Equation 9 generally agrees with the values recommended by Chow *(9)*. However, it calculates higher critical shear stress than does Equation 8. The reason could be that Equation 9 was derived from tests of well-compacted soils (dry density ranging from about 90 to 105 lb/ft^3) and Equation 8 was derived from uncompacted soil tests (dry density ranging from about 60 to 75 lb/ft^3). Compaction increases the resistance of soil to erosion.

A number of erosion equations (*10–12* and Wiggert and Contractor and Cristofano, unpublished data) were developed for estimating embankment erosion. These equations were derived mainly from empirical approximations and limited laboratory and field data. After evaluation of existing erosion equations and the literature review, it was determined that a promising equation for estimating the embankment erosion rate is

$$E = K\ (\tau - \tau_c)^a \tag{10}$$

where

E = the detachment rate per unit area,
τ = the local effective shear stress based on hydraulic conditions,
τ_c = the critical shear stress of soil, and
K and a = empirical coefficients dependent on soil properties.

Three erosion equations were developed for the two types of soil tested in this study and the noncohesive soil tested by McWhorter et al. *(8)*. On the basis of a regression analysis of laboratory data, the following equations were developed:

1. For embankments made from highly cohesive soil such as clay (PI $\geq$ 10)

$$E = 0.000086\ (\tau - \tau_c)^{0.91} \tag{11}$$

2. For embankments made from low-cohesive soil such sandy clay (PI $\leq$ 5)

$$E = 0.00022\ (\tau - \tau_c)^{0.43} \tag{12}$$

3. For embankments made from noncohesive sand or gravel soil

$$E = 0.00324\ (\tau - \tau_c)^{1.3} \tag{13}$$

where E is the erosion rate in cubic feet per second-foot. Figure 7 shows the fitting of the experimental data.

Equations 11–13 were used to generate nomographs for estimating embankment damage caused by flood overtopping as discussed in Development of a Procedure for Determining Embankment Erosion Caused by Flood Overtopping. The experiments for evaluating effects of grass covers on embankment erosion were inconclusive. All of the tests were conducted under free-fall conditions. In tests with low overtopping depths (0.5 ft), the grass-lined embankment appeared to

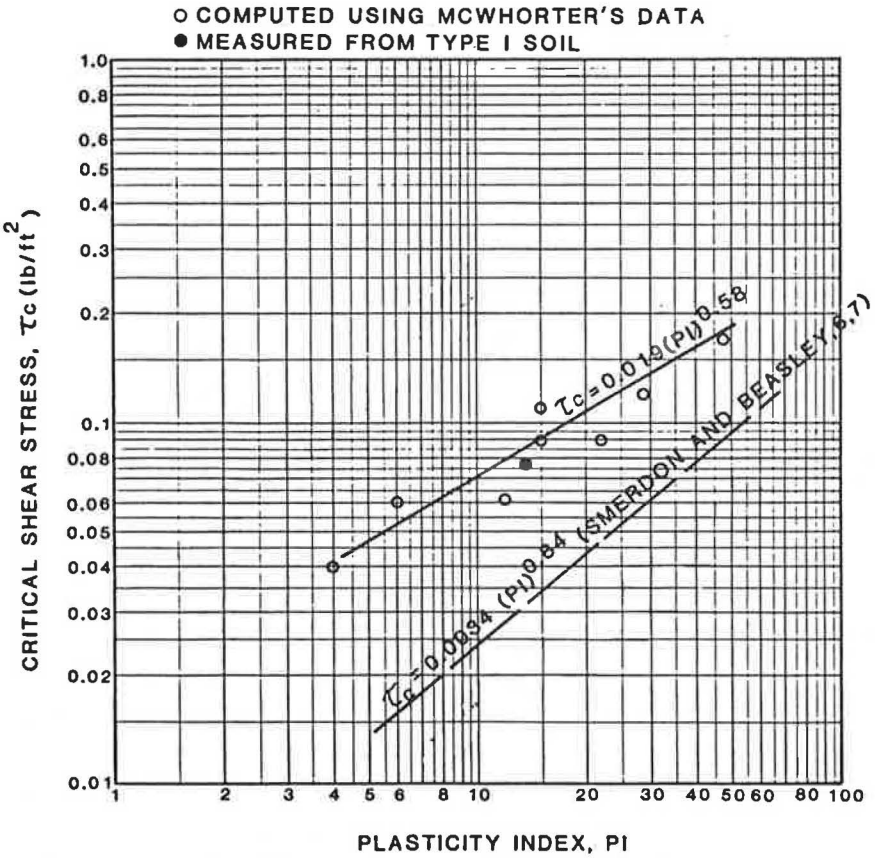

FIGURE 6 Relation of critical shear stress to plasticity index.

perform well. In tests with high overtopping depths (2 and 4 ft), clumps of grass were removed and induced the formation of local scour along the embankment. The nature of the grass cover (clumps versus uniform cover) could induce local scour and increase the shear stress near the clump of grass. A further explanation of this phenomenon could be the existence of weak spots along the embankment or areas in which the root system of the grass was not fully established. Severe toe erosion also occurred. It appeared that these areas of increased erosion, local scour, and toe erosion were related to the erodibility of the underlying soil. Therefore it is reasonable to assume that the erosion equation coefficients K and a for grass cover would be the same as those for the underlying soil and only the τ_c-value would change.

DEVELOPMENT OF A PROCEDURE FOR DETERMINING EMBANKMENT EROSION CAUSED BY FLOOD OVERTOPPING

Development of a Computer Model for Determining Embankment Erosion

A computer model was developed to determine the hydraulic conditions and embankment erosion associated with flood overtopping. Figure 8 is a flowchart of this model. Some of the steps are self-explanatory. Steps 1, 2, 13, and 14 are explained in more detail in the following list.

- Step 1: Divide the modeled embankment into computational sections. The geometry is then input as (x,z) pairs. Manning's n is input for each computational section. Chen and Cotton *(13)* presented values of Manning's n for various surfaces including rigid, soil, rock, grass, and some flexible linings.
- Step 2: Input embankment soil and structure characteristics and erosion equations. A roadway embankment can be considered to contain four layers: pavement, gravel base, grass cover, and base soil. The critical shear stresses and Manning's n-values for the four layers are input as data to the model. Also, the thicknesses of the layers in each computational section are input as data. The developed model can also consider gravel or earth embankments with or without grass and with a homogeneous or nonhomogeneous soil base. When one layer is eroded, the critical shear stress and Manning's n for the immediately lower layer are used for next time-step computation. Equation 10 is used to compute erosion rates. Depending on the characteristics of the layers, proper values of coefficients a and K are input as data.
- Step 13: Determine the erosion rate of each computational section from Equation 10 using the critical shear stress and input coefficients of the erosion equation for the surface layer. If the surface layer was eroded within a period shorter than a computational time step, the critical shear stress of the immediately lower layer would be used for the computation for the remaining time period.

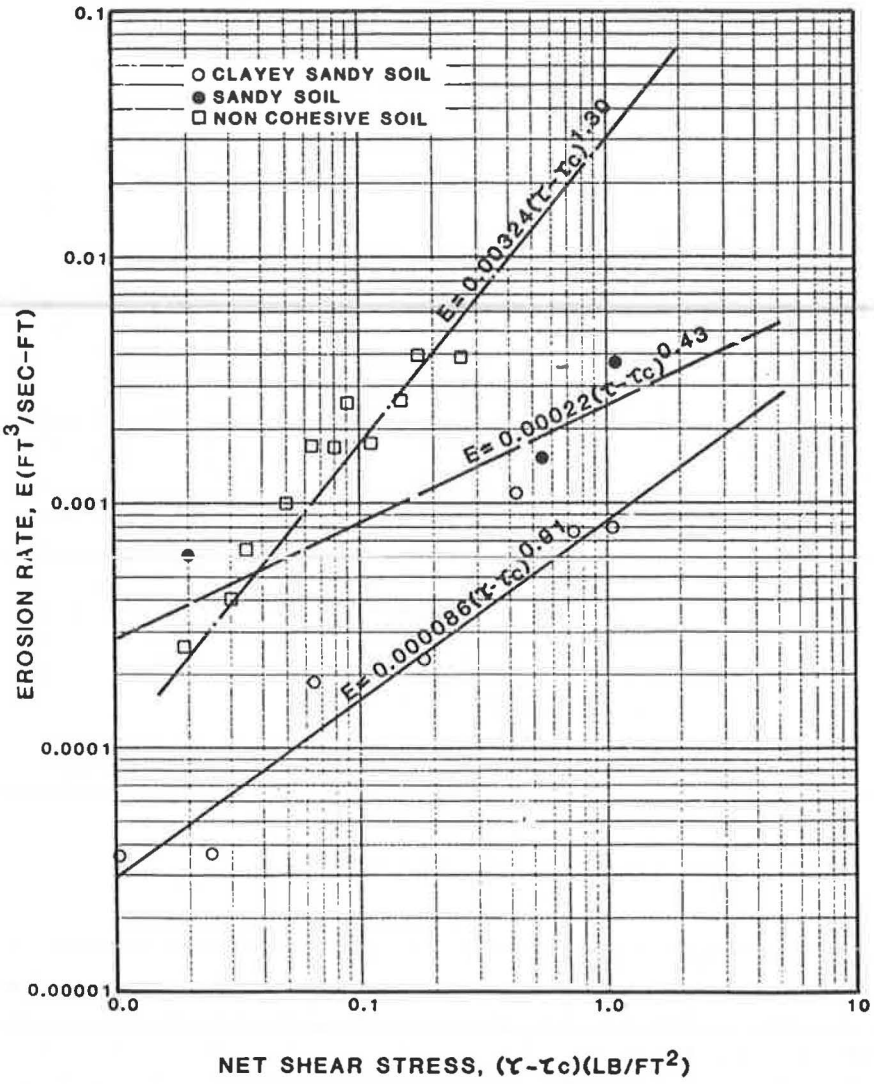

FIGURE 7 Embankment erosion equations.

• Step 14: Determine embankment bed erosion of each section during a time step. For grass, gravel, or the soil surface, the bed erosion depth is

$$\Delta Z = E\ \Delta t \tag{14}$$

where E is the erosion rate from Equation 10 and Δt is the time-step duration. For paved sections, it was assumed that damage to the pavement is not due to direct flow erosion but instead to erosion undermining the roadway base and cantilevering the pavement. Given the condition shown in Figure 9, the maximum normal stress on the pavement due to flow is

$$(\sigma_x)_{max} = M/S_m \tag{15}$$

where M is the bending movement induced by the weight of the pavement and water above a given point and S_m is the section modulus. Let D equal the average depth of flow at the middle of the undermined pavement, t the thickness of the pavement, γ_w the unit weight of water, and γ_a the unit weight of pavement. Then

$$M = (\gamma_w D + \gamma_a t)\ x^2/2 \tag{16}$$

and

$$S_m = t^2/6 \tag{17}$$

Substituting Equations 16 and 17 in Equation 15 yields

$$(\sigma_x)_{max} = [3(\gamma_w\ D + \gamma_a t)\ x^2]/t^2 \tag{18}$$

For the computer model, the undermining length (x) is assumed to be one-tenth of the eroded depth at the edge of the pavement; D is the computed flow depth at the edge of pavement; and γ_w, γ_a, and t are known variables. By substituting these values into Equation 18, $(\sigma_x)_{max}$ is computed. If $(\sigma_x)_{max}$ is larger than the allowable tension stress of the pavement (σ_a), it is assumed that the pavement from the downstream edge to its immediately upstream computational section is eroded within one time step. Then this computation section becomes the downstream edge of the pavement for the next computational step.

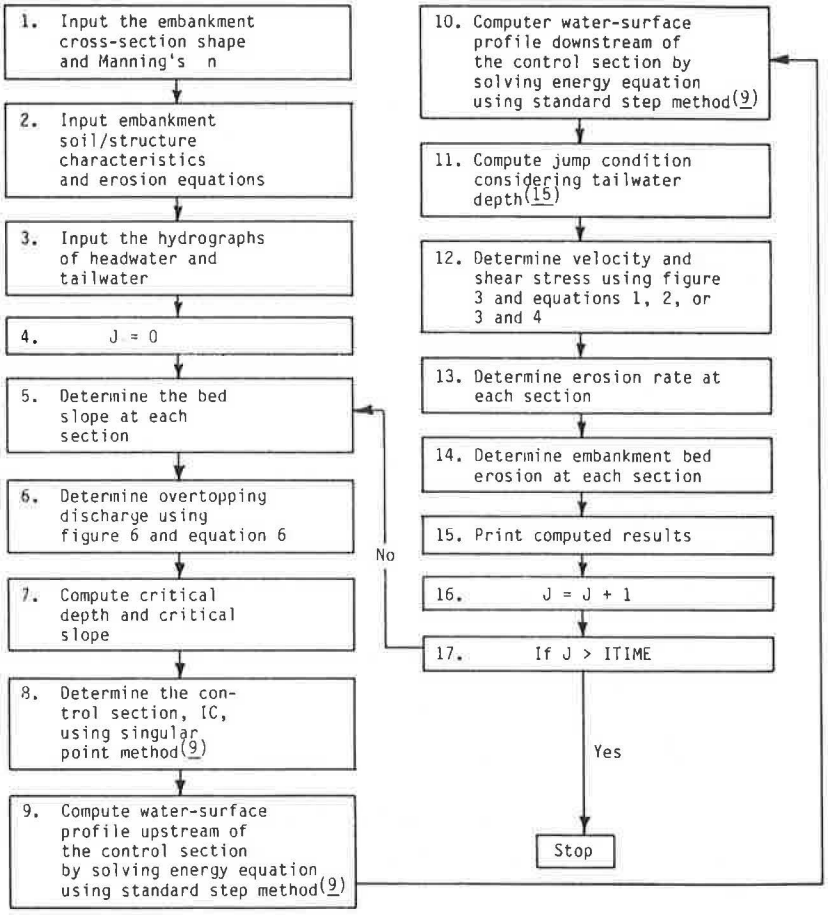

FIGURE 8 Flowchart of the computer model EMBANK.

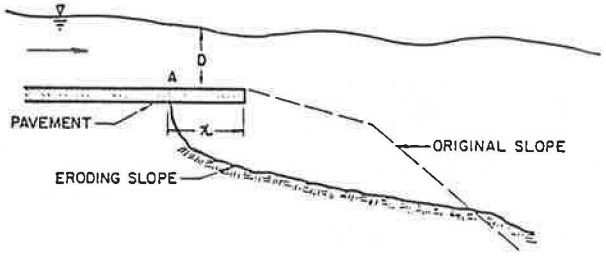

FIGURE 9 Undermining of embankment pavement.

Calibration of the Computer Model

The bare-soil embankment test data from the initial laboratory tests were used to calibrate the computer model. The geometry and soil characteristics of these embankments and overtopping headwater and tailwater depths were input to the computer program to calculate the volume of material eroded during the first hour. Then the calculated values were compared with the measured volumes during the first hour of the tests and plotted in Figure 10. The agreement is acceptable. The model was then used to develop nomographs for estimating embankment damage under various flow and embankment conditions.

Development of Nomographs for Determining Embankment Erosion Caused by Flood Overtopping

The calibrated computer model was applied to develop nomographs for estimating erosion of bare-soil and pavement embankments with and without vegetal cover under the following conditions:

- Base soils consisting of high-cohesive material, low-cohesive material, and noncohesive material;
- Paved embankment with and without Class A, C, and E grass covers;
- Embankment heights ranging from 2.5 to 15 ft;
- Overtopping depths ranging from 1 to 10 ft; and
- Ratio of tailwater depth to overtopping depth ranging from free fall to 0.9.

The computed erosion rates (averaged over a 4-hr period) were plotted in Figure 11 for 5-ft high-cohesive (PI = 13) and low-cohesive (PI = 5) bare-soil embankments and in Figure 12 for 5-ft noncohesive soil embankments ($d_{50} \cong 4$ mm). These two figures can be used to estimate erosion rates of 5-ft bare-soil embankments. Because critical shear stress is not a particularly sensitive parameter, it is suggested that Figure 11 be applied to high-cohesive soil embankments with PI $\geq$ 10 and to low-cohesive soil embankments with PI $\leq$ 5. Figure 12 should be applied to noncohesive soil embankments with $d_{50} < 8$ mm. For embankment soils with PI between 5 and 10, the erosion rate can be determined by interpolation.

Other factors considered in the procedure include the effects of pavement and grass, the duration of overtopping, and the height of the embankment. Under high tailwater conditions, most erosion of the bare-soil embankment occurred along the top and downstream shoulder. Addition of a paved surface

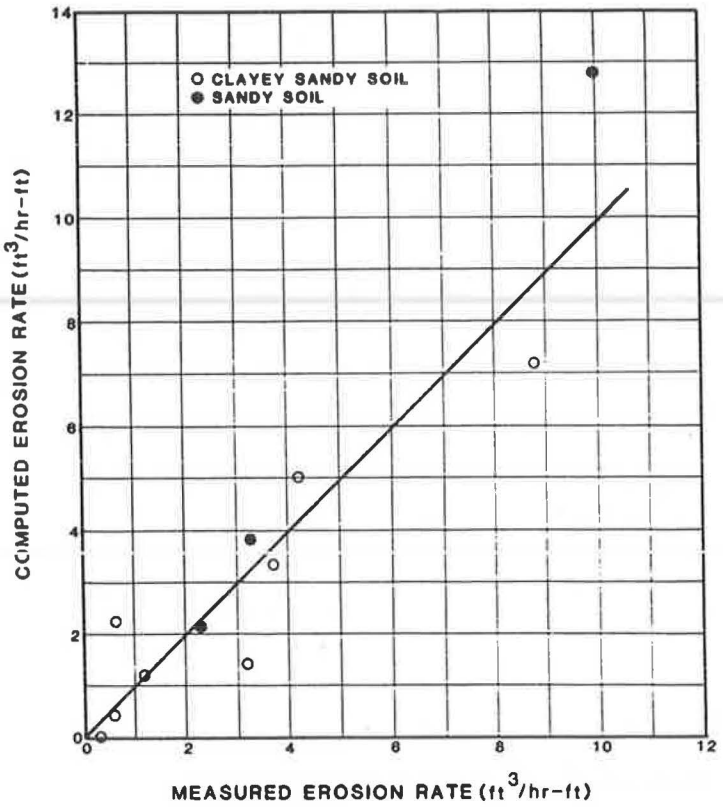

FIGURE 10 Computed versus measured erosion rate.

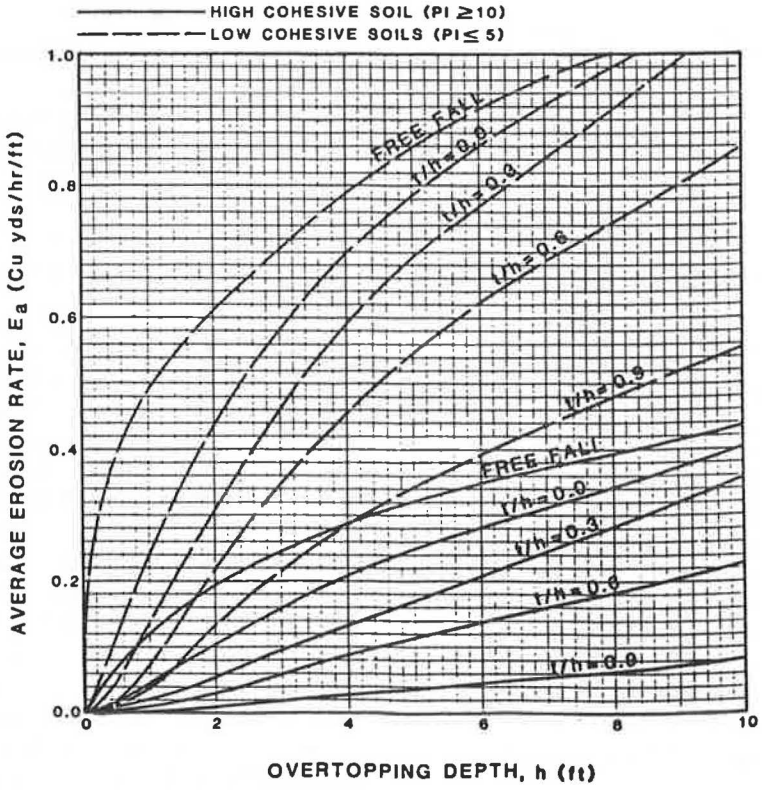

FIGURE 11 Average erosion rate during 4-hr overtopping of 5-ft cohesive bare-soil embankment.

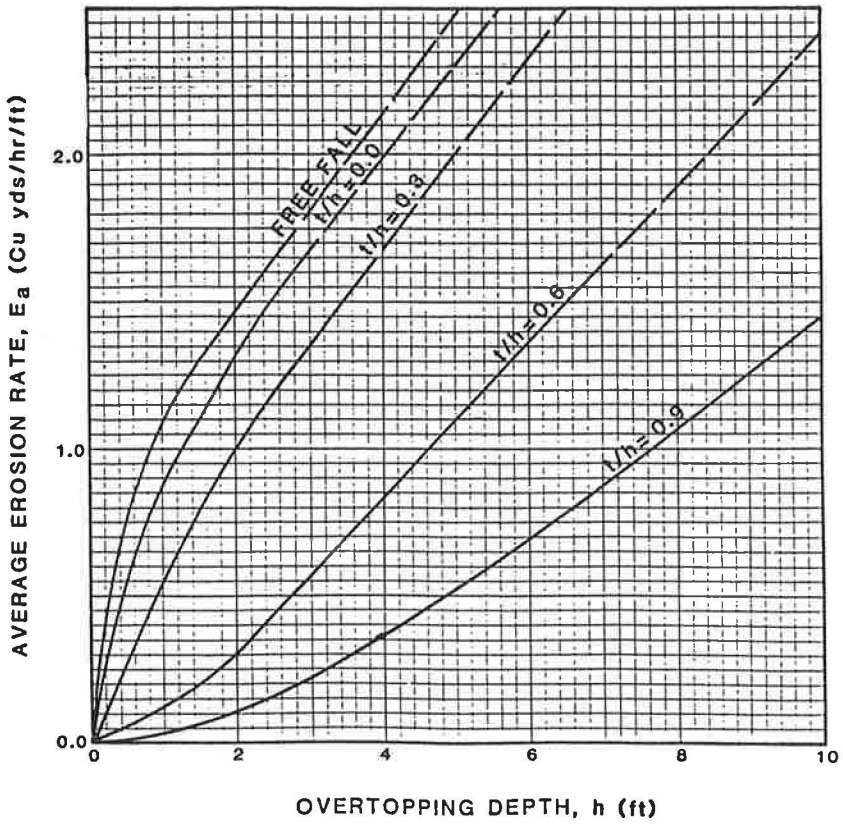

FIGURE 12 Average erosion rate during 4-hr overtopping of 5-ft noncohesive bare-soil embankment.

reduced the eroded area. The tests conducted in the study showed that erosion was reduced by as much as 50 percent with high tailwater. When tailwater was low, most erosion occurred near the downstream toe of the embankment, and the effect of pavement on embankment erosion was not as significant. A number of nomographs were generated using the computer model for estimating the average erosion rate of paved 5-ft-high embankments with and without vegetal cover on the embankment slopes. Depending on the type of fill material and the vegetation conditions, pavement coupled with vegetation cover reduced embankment erosion from 10 to 50 percent. Figure 13 shows an example of an erosion rate of a paved embankment with grass cover. The complete set of nomographs was presented by Chen and Anderson *(14)*.

The laboratory test data clearly showed that the erosion rate reduced with time. Figure 14 shows approximated relations of $\bar{E}/E_a$ versus time, based on laboratory test data, where $\bar{E}$ is the average erosion rate over a test time period and E_a is the erosion rate during the first 4 hr. With high tailwater, the water-surface profile of overtopping flow is controlled by the tailwater and remains about the same throughout the erosion of the embankment. Therefore velocity and shear stress generally decrease during the progress of embankment erosion and thereby decrease the erosion rate. With low tailwater and free-fall conditions, the reduction in erosion rate with time is less. Figure 15 shows the adjustment factor when the embankment height varies from 5 ft. Embankment erosion increases with increases in embankment height.

Figure 11, 12, or 13, coupled with Figures 14 and 15, can be applied for estimating an embankment erosion rate using the following procedure:

1. Find out the type of embankment base soil (high-cohesive, low-cohesive, or noncohesive soil), embankment height, paved or nonpaved surface, and type of vegetal cover.
2. Select the headwater depth (h), tailwater depth (t), and duration (T) for a design flood.
3. Compute t/h.
4. With h and t/h enter Figure 11 (for cohesive bare soil), Figure 12 (for noncohesive bare soil), Figure 13 (for paved cohesive-soil embankment with Class A grass cover), or other nomographs (not shown in this paper for paved embankments) to determine the erosion rate (E_a) for a 5-ft embankment. A rough estimate of the effect of pavement and vegetation is a 30 percent reduction of bare-soil embankment erosion for a surface-flow condition and a 10 percent reduction for a plunging-flow condition, if the flow shear on the slope is larger than the critical shear stress of the vegetated embankment.
5. Determine adjustment factor K_1 from Figure 14 considering the design flood duration (T).
6. Determine K_2 from Figure 15 if the embankment height is different than 5 ft.
7. Compute the average erosion rate over the design flood duration:

$$\bar{E} = K_1 K_2 E_a \tag{19}$$

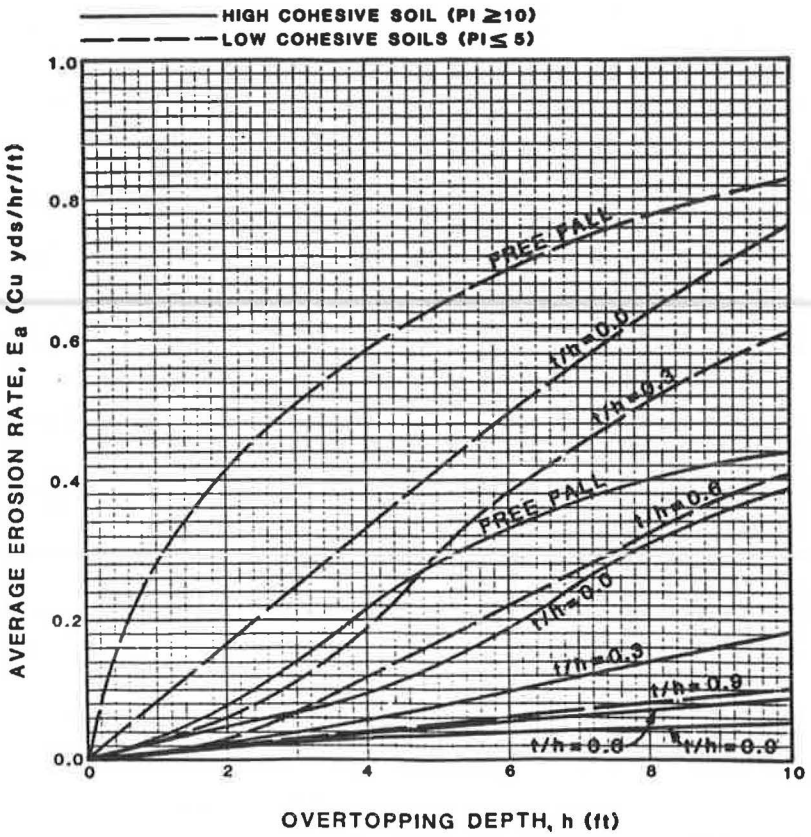

FIGURE 13 Average erosion rate during 4-hr overtopping of 5-ft paved cohesive soil embankment with Class A vegetal cover.

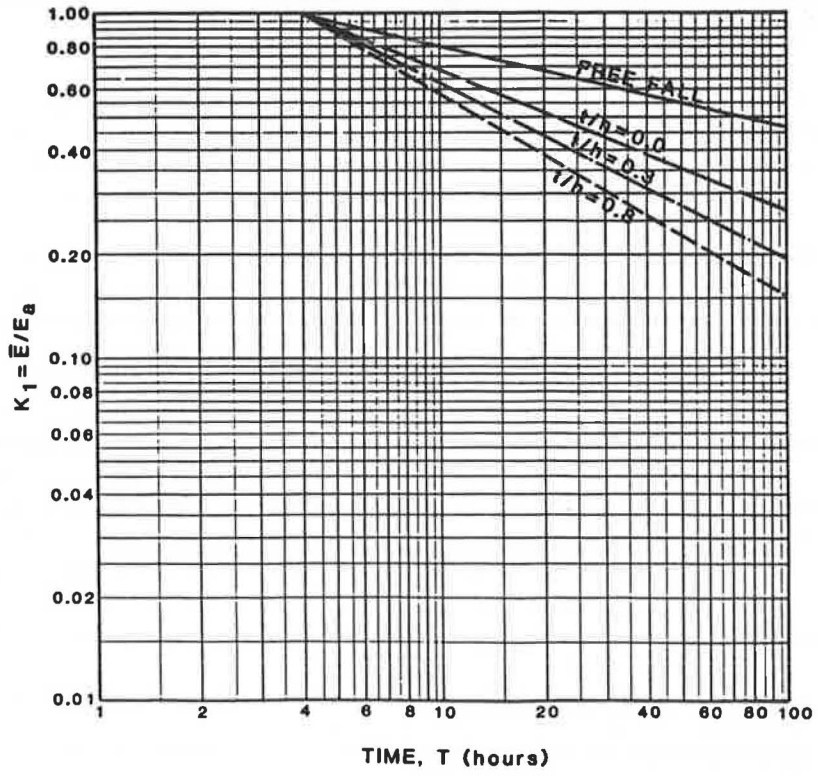

FIGURE 14 Average erosion rate change with changes in duration.

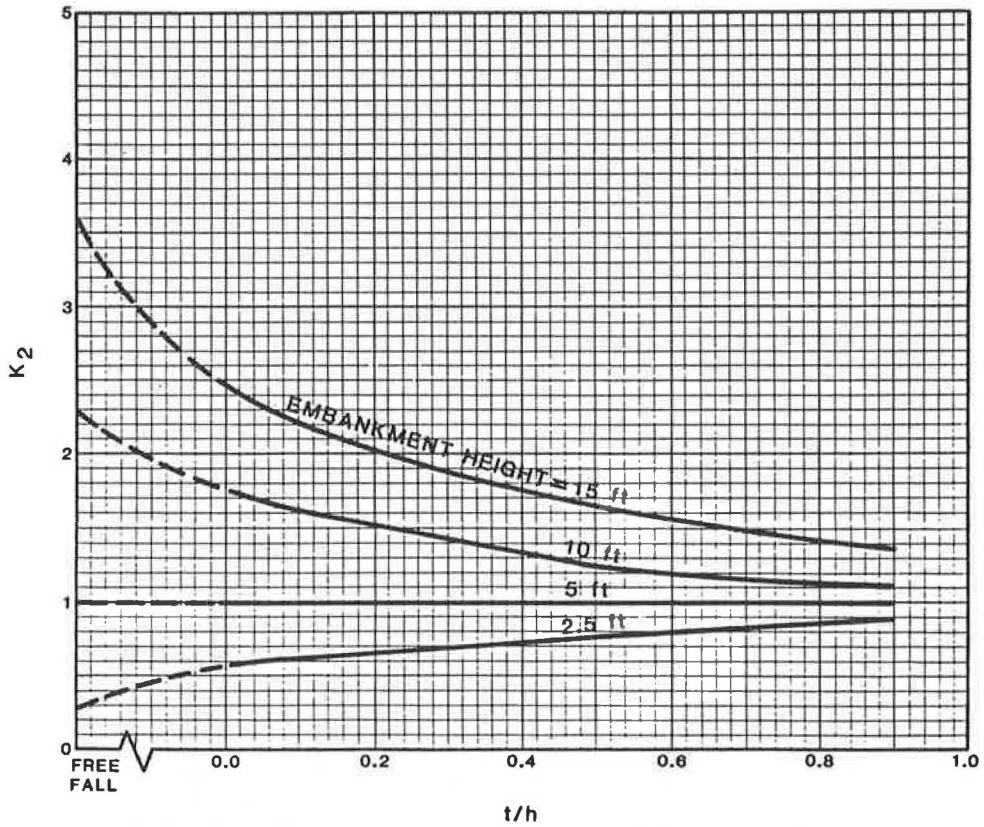

FIGURE 15 Adjustment factor taking embankment height into consideration.

8. Compute the total erosion volume:

$$V_s = ET \tag{20}$$

The procedures described were applied to the laboratory test data and the field data collected during this project. The estimated results are compared with measured erosion rates in Figure 16. The agreement is reasonably good. This indicates that the developed nomographs are useful for estimating embankment erosion rates with reasonable accuracy. However, only limited soil bases were considered in developing these nomographs, and the effects of pavement and grass were evaluated by using limited laboratory data. Therefore, for other types of embankments or for more detailed estimation of embankment erosion, the computer model developed as part of this study should be used. It is recommended that the nomographs and developed computer model be further verified or modified, or both, using additional field and laboratory data.

EVALUATION OF EMBANKMENT PROTECTION MEASURES

This study evaluated the effectiveness of several erosion protection measures, including vegetated embankments and embankments protected with gabion mattresses, soil cement, geoweb, and enkamat.

For each protective measure tested, a preliminary assessment of the failure mechanism or threshold conditions for failure of the protective measure was conducted. The failure signal was identified as a noticeable change in the water surface during the test or noticeable erosion of the protective measure or embankment material after the test.

The failure mechanism associated with the gabion mattresses appears to be related to the movement of the rocks within the mattress. The moment when the liner becomes exposed was construed as the threshold condition for failure. In general, gabion mattresses performed quite well and in no instance was the embankment in danger of erosion.

The potential failure mechanisms associated with soil cement were initially identified as the presence of surface cracks or the undermining of the layer of soil cement at the toe of the embankment. Because of the nature of the tests, neither failure mechanism was realized. A number of cycles involving freezing and thawing or wetting and drying of the soil cement layer are the catalyst needed for surface cracks to form. The relatively short testing period prevented this effect. In general, the soil cement protective measure performed quite well. After 10 hr of testing under the most severe conditions, no erosion was evident in either the soil cement or the embankment material.

For the geoweb grid confinement system, the failure mechanism appears to be associated with the boiling of rocks out of the cells of the geoweb. As the rocks are boiled out, the flow velocity directly impinges on the geoweb structure and creates an elongation of the geoweb section. The elongation effect, in turn, exposes the embankment material to direct erosion by the flowing water. In general, the geoweb performed poorly in the configuration tested by this study. Attempts were made to improve the stability of the protective measure by increasing the length and number of staples in the geoweb system. In addition, the configuration of the geoweb system was changed.

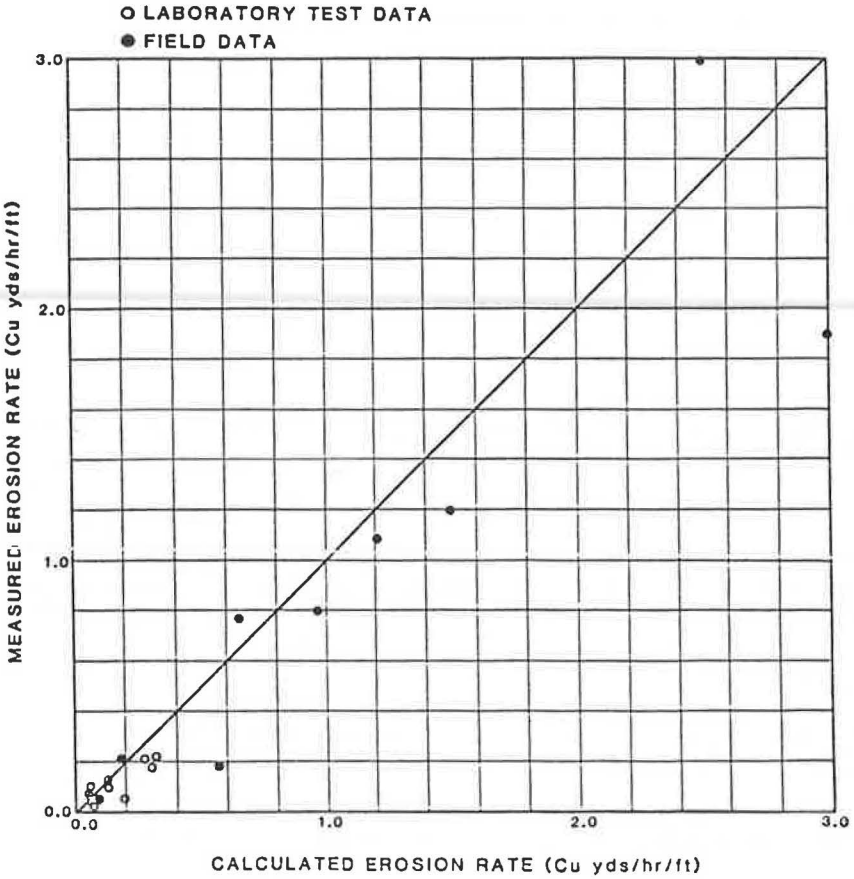

FIGURE 16 Comparison of calculated and measured embankment damage data.

The failure mechanism associated with enkamat was related to ripping or stretching of the enkamat material or noticeable erosion of the embankment beneath the enkamat. The presence of grass in the enkamat had little effect. This resulted from an unsatisfactory stand of grass (density and length) after a growth period of only 1 year. Because of the relatively short growth period, the root system was not fully developed. In all tests, erosion of the embankment material occurred as the flow velocity increased with overtopping depths greater than 1 ft. In general, enkamat afforded reasonably good erosion protection during the tests of low overtopping depths. As the overtopping depths increased beyond 1 ft, erosion of the embankment appeared to be accelerated by the presence of the enkamat.

For grass-lined embankments, the failure mechanism was associated with direct erosion or loss of grass. In tests with low velocities and overtopping depths (0.5 ft), the grass-lined embankment appeared to perform well. In tests with overtopping depths greater than 0.5 ft, pockets of grass were removed and induced local scour along the embankment. In addition to the local scour, severe toe erosion occurred during the tests involving overtopping depths of 2 and 4 ft. Although grass-lined slopes usually retard flow velocity and reduce erosion, these tests did not confirm those results.

In summary, erosion of the geoweb system started when the flow velocity exceeded 8.0 ft/sec. Rocks within each gabion were observed to migrate as the flow velocity exceeded 15 ft/sec. However, gabion still provided sufficient protection during the 15-hr testing period. Even at velocities in excess of 20 ft/sec, no failure of soil cement was observed. Damage to the enkamat material was observed when the flow velocities exceeded 10 ft/sec. The critical velocities associated with the various protective measures, as determined by the tests conducted, are given in Table 1. Table 2 gives the critical shear stress recommended by Chen and Cotton *(13)* for gabion, enkamat, and grass.

TABLE 2 CRITICAL VELOCITY ASSOCIATED WITH PROTECTIVE MEASURES

Protective Measure	Overtopping Depth (ft)	Critical Velocity (ft/sec)	Critical Shear Stress (lb/ft^2)
Geoweb	0.9	6.0	0.7
Gabion	4.0	15.0	4.0
Soil cement	4.0	>20.0	
Enkamat	2.0	10.0	2.0
Grass	Varies	Varies	Varies

ACKNOWLEDGMENTS

This work was supported by the FHWA, U.S. Department of Transportation, and the U.S. Department of Agriculture Forest Service. State highway agencies of Arizona, Arkansas, Missouri, and Wyoming, and the U.S. Geological Survey assisted in gathering field data. The writers wish to express their appreciation to J. Sterling Jones for his valuable comments and

suggestions. They also acknowledge the assistance of Mike Mussetter in handling embankment construction and data collection and that of George K. Cotton and Rebecca Summer in literature search and review.

REFERENCES

1. Simons, Li and Associates, Inc. *Presentation of Field Data on Embankment Damage Due to Flood Overtopping*. Progress Report for Task A. FHWA, U.S. Department of Transportation, Jan. 1984.
2. H. W. Hjalmarson. *Flood Characteristics and Highway Damage at Five Arizona Sites, Flood of October 1983*. U.S. Geological Survey; FHWA, U.S. Department of Transportation, Tucson, Ariz., Sept. 1984.
3. C. E. Kindsvater. Discharge Characteristics of Embankment-Shaped Weirs. USGS Water-Supply Paper 1617-A. *Studies of Flow of Water Over Weirs and Dams*, U.S. Geological Survey, 1964.
4. J. N. Bradley. *Hydraulics of Bridge Waterways*. Hydraulic Design Series 1. FHWA, U.S. Department of Transportation, 1973.
5. J. Gessler. Beginning and Ceasing of Sediment Motion. In *River Mechanics*, edited and published by H. W. Shen, Fort Collins, Colo., 1971, Chapter 7.
6. E. T. Smerdon and R. P. Beasley. Relation of Compaction and Other Soil Properties to Erosion Resistance of Soils. *Transactions*, ASCE, Vol. 8, 1959.
7. E. T. Smerdon and R. P. Beasley. *The Tractive Force Theory Applied to Stability of Open Channels in Cohesive Soils*. Research Bulletin 715. Agricultural Experiment Station, College of Agriculture, University of Missouri, Columbia, Oct. 1959.
8. J. C. McWhorter, T. G. Carpenter, and R. N. Clark. *Erosion Control Criteria for Drainage Channels*. Mississippi State Highway Department, Jackson; FHWA, U.S. Department of Transportation; Agricultural Experiment Station, Mississippi State University, State College, March 1968.
9. V. T. Chow. *Open-Channel Hydraulics*. McGraw-Hill Book Company, New York, 1959.
10. R. Ariathurai and K. Arulanandan. Erosion Rates of Cohesive Soils. *Journal of the Hydraulics Division*, ASCE, Vol. 104, No. HY2, Feb. 1978, pp. 279–283.
11. S. P. Chee. Design of Erodible Dams. *Proc., International Conference of Water Resources Engineering*, Asian Institute of Technology, Bangkok, Thailand, Vol. 1, 1978, pp. 105–113.
12. V. R. Schneider and K. V. Wilson. *Hydraulic Design of Bridges with Risk Analysis*. Report FHWA-TS-80-226, FHWA HDV-21. U.S. Geological Survey; Office of Development, FHWA, U.S. Department of Transportation, March 1980.
13. Y. H. Chen and G. K. Cotton. *Design of Roadside Channels with Flexible Linings*. Hydraulic Engineering Circular 15. FHWA, U.S. Department of Transportation, Feb. 1986.
14. Y. H. Chen and B. A. Anderson. *Development of a Methodology for Estimating Embankment Damage Due to Flood Overtopping*. Simons, Li & Associates, Inc., Fort Collins, Colo.; FHWA, U.S. Department of Transportation; U.S. Department of Agriculture Forest Service, March 1986.

Channel Evolution in Modified Alluvial Streams

ANDREW SIMON AND CLIFF R. HUPP

Modification of alluvial channels in western Tennessee has created increased energy conditions along main stems and tributaries and initiated longitudinal channel adjustment. Changes in bed level are functions of the magnitude and extent of the imposed disturbance and the location of the adjusting reach in the fluvial network. Streambed degradation is described by simple power equations. Computed exponents define the magnitude of downcutting with time and decrease nonlinearly with distance upstream from the area of maximum disturbance (AMD). Aggradation begins immediately in reaches downstream of the AMD and in upstream reaches after overadjustment by the degradation process. Aggradation rates increase linearly with distance downstream from the AMD and can be estimated from local degradation rates. Channel widening by mass wasting follows degradation and continues through aggradational phases. Piping in the loess-derived bank materials enhances bank failure rates by internally destabilizing the bank. Development of the bank profile is defined in terms of three dynamic and observable surfaces: (*a*) vertical face (70 to 90 degrees), (*b*) upper bank (25 to 50 degrees), and (*c*) slough line (20 to 25 degrees). The slough line develops through additional flattening by low-angle slides and fluvial reworking and is the initial site at which riparian vegetation and stable bank conditions are reestablished. A six-step, semiquantitative model of channel evolution in disturbed channels was developed by quantifying bed level trends and recognizing qualitative stages of bank slope development.

Alluvial channels adjust to imposed changes so as to offset the effects of those changes and approach quasi-equilibrium. Lane *(1)* describes this general balance in terms of the stream power expression

$$QS \propto Q_s d_{50} \quad (1)$$

where

- Q = water discharge, in cubic meters per second;
- S = channel gradient, in meters per meter;
- Q_s = bed material discharge, in kilograms per cubic meter; and
- d_{50} = median grain size of bed material load, in millimeters.

Dredging and straightening (shortening) alter both channel cross-sectional area and channel gradient (S) such that they are increased. By Equation 1, this results in a proportionate increase in either bed load discharge (Q_s), or bed material size (d_{50}), or both, such that rapid and observable morphologic changes occur.

Channelization (dredging and straightening) is a common engineering practice for controlling flooding or draining wetlands. Quantification of subsequent channel responses can be valuable in estimating the effects on river-crossing structures and lands adjacent to these channels. The purposes of this study are (*a*) to assess the channel changes and network trends of bed level response after modifications between 1959 and 1972 of alluvial channels in western Tennessee (Figure 1) and (*b*) to develop a conceptual model of bank slope development to qualitatively assess bank stability and potential channel widening. Such a model will be useful in identifying trends of alluvial channel stability.

STUDY AREA

Western Tennessee is an area of approximately 27,500 km^2 bounded by the Mississippi River on the west and the Tennessee River on the east (Figure 1). All of the stream systems studied drain to the Mississippi River via the Obion, Forked Deer, and Hatchie river basins. These rivers are cut into unconsolidated and highly erosive formations *(2)*, predominantly of Quaternary age. Wisconsin loess dominates the surficial geology of the region, and a majority of the channels have medium-sand beds. These alluvial channels are free to systematically adjust their profiles after a disturbance because of the lack of bedrock control of local base level.

DATA COLLECTION

Channel morphology data were collected and compiled from previous surveys to determine channel change with time. These data consisted of bed elevations and gradients; channel top widths; and channel lengths before, during, and after modification. If they were available, gauging station records were used to record annual changes in water surface elevation at a given discharge *(3)*. Changes in water surface elevation at the given discharge imply similar changes on the channel bed and can be used to document bed level trends *(3, 4)*.

Identification and dating of various geomorphic surfaces can be useful in determining the relative stability of a reach and the status of bank slope development *(5, 6)*. Data collection involved locating and dating riparian vegetation on (*a*) newly stabilized surfaces to determine the timing of initial stability for that surface and (*b*) unstable bank surfaces to estimate rates of bank retreat.

U.S. Geological Survey, A-413 Federal Building, U.S. Courthouse, Nashville, Tenn. 37203.

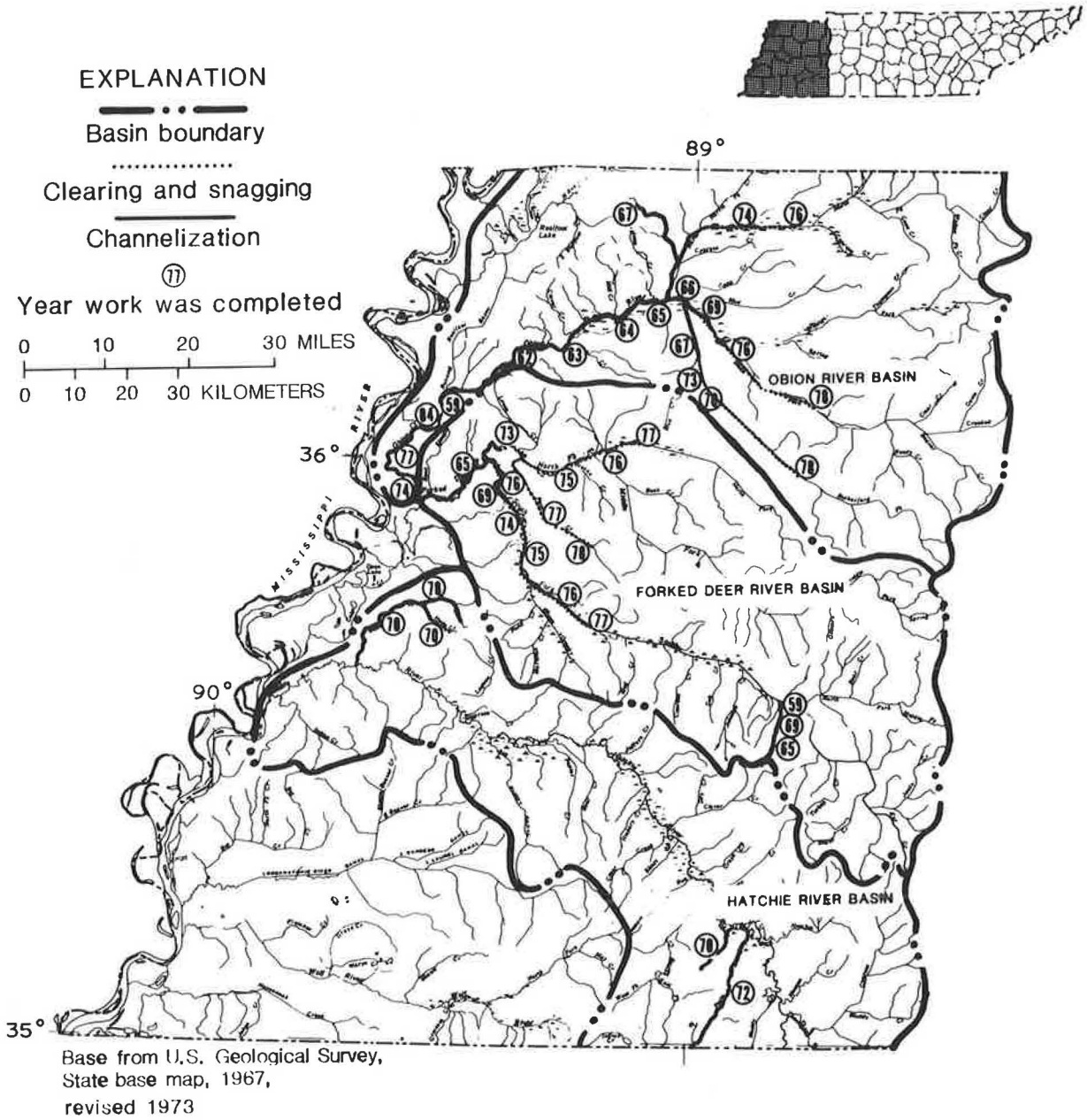

FIGURE 1 Channel modifications in western Tennessee.

BED LEVEL RESPONSE

Adjustments in modified western Tennessee channels and their tributaries include incision, headward erosion, downstream aggradation, and bank instabilities. Previous investigations *(3)* identified adjustments to gentler gradients and reduced energy conditions. These studies provided empirical time-based relations of site-specific gradient adjustment. These studies further determined that the bed of the Hatchie River had remained stable during the period when streams of the Obion and Forked Deer river basins were undergoing drastic morphologic changes.

Bed level adjustment trends at gauged sites are determined by calculating the mean annual specific-gauge elevation for the period just before and following channelization activities *(3, 4)*. Specific-gauge trends serve as examples for the ungauged, but periodically surveyed, sites *(7)*. The processes of aggradation and degradation at a site, through time, are described by simple power equations that take the general form

$$E = a\,(t)^b \tag{2}$$

where

- E = elevation of the bed or specific gauge for a given year, in meters above sea level;
- a = premodified elevation of the bed or specific gauge, in meters above sea level;
- t = time since channel work, in years, where $t_0 = 1.0$; and
- b = exponent determined by regression, indicative of the nonlinear rate of change on the bed.

TABLE 1 SITES WITH CALCULATED GRADATION RATES (b)

Stream	b	n	r2	RKM	TO	DA
Cane Creek						
	-0.01620	7	0.99	23.89	1969	87.8
	0.00168	2	1.00	23.89	1980	87.8
	-0.02022	4	1.00	20.24	1969	130
	0.01052	2	1.00	20.24	1980	130
	-0.03300	3	1.00	14.46	1969	169
	0.00770	2	1.00	14.46	1980	169
	-0.03131	2	1.00	10.09	1969	187
	0.00352	2	1.00	10.09	1980	187
	-0.04126	3	0.91	6.53	1969	207
	-0.02011	4	0.92	4.06	1969	217
	0.00835	2	1.00	4.06	1980	217
Cub Creek						
	-0.00243	3	0.69	11.13	1969	2.8
	-0.00342	3	0.87	9.22	1969	17.1
	-0.00565	4	0.88	3.48	1969	37.0
	-0.00905	5	0.91	2.48	1969	38.9
	0.00272	2	1.00	2.48	1976	38.9
Hoosier Creek						
	-0.00843	3	1.00	8.29	1967	39.4
	-0.01130	4	0.94	4.81	1966	69.4
	-0.02081	3	0.67	0.88	1965	84.7
	0.00274	2	1.00	0.88	1968	88.8
	-0.02630	3	0.99	0.02	1965	88.8
Hyde Creek						
	0.00281	2	1.00	3.81	1975	16.6
	-0.00737	2	1.00	3.81	1969	16.6
	-0.01070	4	0.92	2.22	1969	23.1
	-0.01380	3	0.99	1.19	1969	26.2
	-0.02050	4	1.00	0.02	1969	27.7
Meridian Creek						
	-0.00326	3	0.99	5.94	1965	38.3
	-0.00580	4	0.98	4.73	1964	39.6
	-0.00341	3	0.99	2.41	1969	49.2
	-0.00190	3	0.99	1.54	1967	50.2
North Fork Forked Deer River						
	-0.00740	4	0.95	38.46	1977	448
	-0.01076	5	0.52	32.47	1974	479
	-0.00839	4	0.96	30.28	1978	552
	-0.01720	10	0.95	8.53	1973*	2432
	-0.02297	3	0.87	6.16	1972	2440
North Fork Obion River						
	0.00111	15	0.69	59.37	1969*	422
	-0.00206	2	1.00	42.48	1979	741
	-0.00490	2	1.00	33.95	1975	922
	-0.00372	13	0.80	28.96	1972*	963
	-0.01240	6	0.93	15.83	1965*	1243
	-0.02470	4	0.85	9.49	1965*	1303
	0.00303	5	0.89	9.49	1967*	1303
Obion River						
	-0.02220	10	0.95	110.22	1965*	1948
	0.00463	10	0.74	110.22	1974*	1948
	-0.04030	4	0.81	100.08	1965*	4496
	0.00235	16	0.76	100.08	1968*	4496
	0.00908	19	0.93	86.40	1965*	4797
	0.00518	15	0.84	55.03	1963*	5265
	0.00585	16	0.74	33.47	1960*	6229
Pond Creek						
	-0.00828	5	0.81	18.29	1977	96.9
	-0.00799	4	0.84	15.80	1977	117
	-0.01233	4	0.97	11.78	1977	140
	-0.00900	5	0.79	1.71	1977	176
Porters Creek						
	-0.01069	7	1.00	27.51	1971	37.8
	-0.01320	7	0.99	18.02	1971	92.7
	-0.00578	6	1.00	14.30	1971	105
Rutherford Fork Obion River						
	0.00149	19	0.60	48.11	1965*	285
	-0.00317	4	0.91	28.80	1977	521
	-0.00493	3	1.00	24.46	1977	557
	-0.00991	4	0.79	16.73	1972	616
	0.00356	4	0.99	16.73	1977	616
	-0.01728	9	0.93	7.88	1965*	692
	0.00433	9	0.88	7.88	1974*	692
South Fork Forked Deer River						
	-0.00895	6	0.59	44.41	1976	1992
	-0.00950	10	0.92	26.23	1974*	2414
	-0.00978	5	0.76	21.40	1969	2598
	-0.01264	5	0.96	19.15	1969	2616
	-0.01630	15	0.94	12.71	1969*	2639
	0.01180	13	0.92	5.31	1969*	2727
South Fork Obion River						
	0.00133	13	0.90	55.35	1969*	528
	-0.00054	4	0.26	45.70	1972	811
	-0.00238	6	0.50	37.33	1972	914
	-0.00661	7	0.90	30.89	1977*	922
	-0.00573	5	0.87	27.03	1972	1020
	-0.00932	4	0.94	18.34	1972	1093
	-0.02430	11	0.87	9.33	1965*	1948
	0.00544	9	0.88	9.33	1975*	1948

Note: b, nonlinear gradation rate; n, number of observations; r2, coefficient of determination; RKM, river kilometer; TO, start of observed gradation process; DA, drainage area in square kilometers; *, specific gauge data used.

Equation 2 reflects bed level response at a site (Table 1) and implies that adjustment rates are initially rapid and then diminish as the bed elevation asymptotically approaches a condition of no net change (Figure 2). The magnitude of b denotes the nonlinear rate of degradation (negative b) or aggradation (positive b) and is used as the dependent variable in regression analyses for determination of longitudinal adjustment trends.

Degradation exponents ($-b$) generally range from -0.005 to -0.040 with the greatest rates of change occurring near the upstream side of the area of maximum disturbance (AMD), usually the upstream terminus of the channel work. Increases in downstream channel gradient and cross-sectional area by man result in a stream power that is more than sufficient to transport the bed material delivered from upstream. The bed of the channel therefore erodes headward to increase bed material transport or reduce channel gradient, or both. Typically, degradation occurs for 10 to 15 years at a site and can deepen the channel as much as 6.1 m.

Aggradation rates ($+b$) are less than their degradation counterparts and generally range from 0.001 to 0.009 with the greatest rates occurring near the stream mouth. This process begins immediately after channelization downstream of the AMD, may reach 0.12 m/year, and can continue for more than 20 years. As degradation proceeds upstream from the AMD to reduce channel gradient, aggradation downstream of the AMD similarly flattens gradients as part of an integrated basin response to the man-induced increases in energy conditions *(7)*.

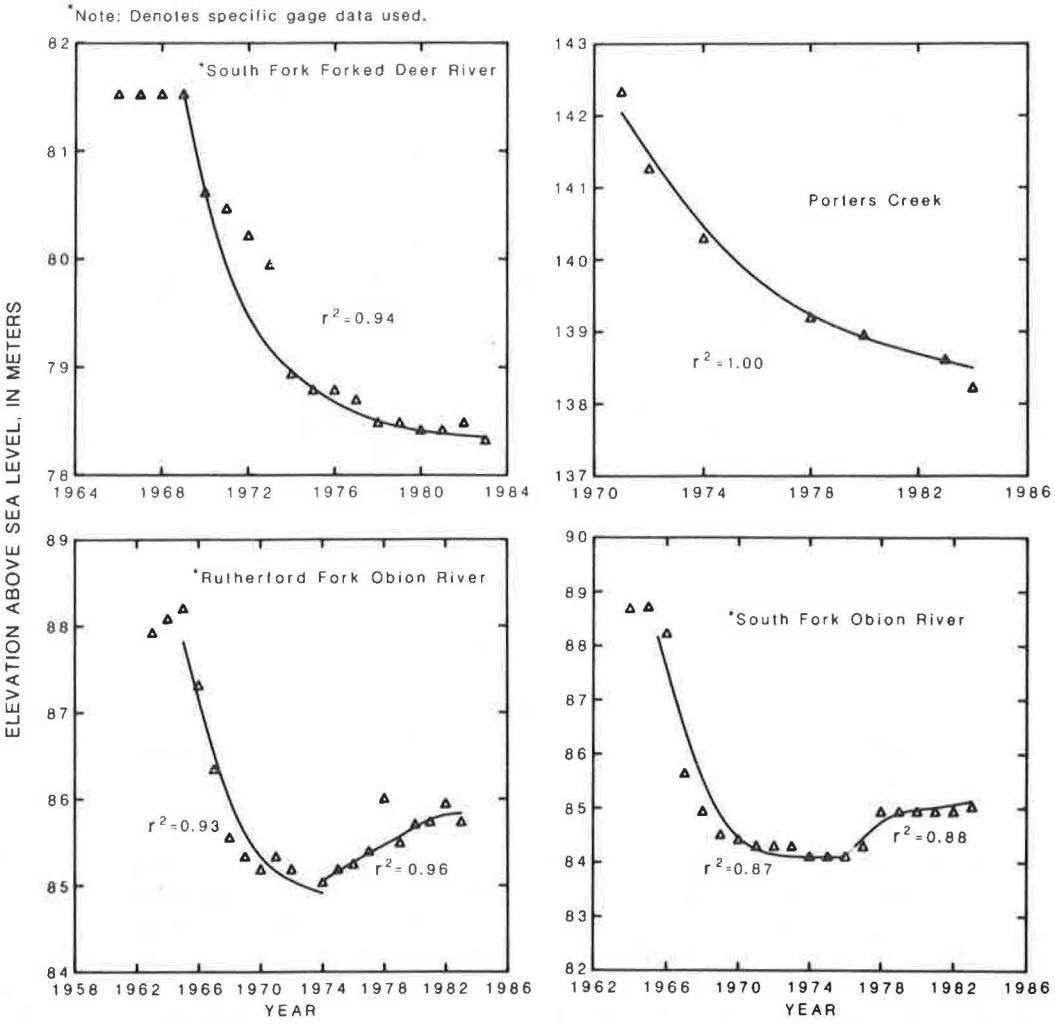

FIGURE 2 Examples of fitting power equations to degradation and aggradation trends through time.

Aggradation also occurs at sites upstream of the AMD that have been previously degraded and suggests an initial overadjustment by degradation. This secondary aggradation occurs as headward infilling. The rate of infilling at a site is approximately 78 percent less (S_E = 2.85) than the initial rate of degradation at that site *(7)*. Expected aggradation rates at sites upstream of the AMD can therefore be estimated at approximately 22 percent of the degradation rate at the site in question. Equations have been developed to calculate aggradation rates in the Cane Creek and Forked Deer and Obion river systems and are reported in Simon *(7)*.

Degradation rates decrease nonlinearly with distance upstream from the AMD in the Cane Creek and Forked Deer and Obion river basins as values of b become less negative and approach 0.0 (Figure 3). Linear relations are derived from these trends and used to predict degradation rates in the three basins *(7)*. The shapes of the curves that represent areal trends of degradation are functions of the magnitude and extent of the imposed disturbance.

Completed and ongoing rates of bed level change as a function of distance upstream from the mouth of the Obion River are shown in Figure 4. Rates of bed level change are plotted on the y-axis; the horizontal 0.00 line represents the threshold of critical power and, theoretically, no net change on the channel bed *(8)*. Deviations from the 0.00 line denote a period of bed level change caused by the imposed disturbance or by subsequent channel responses. The Obion River is used as a typical example of bed level response. Similar models have been documented for other streams and basins in western Tennessee *(7)*.

The modifications imposed on the Obion River can be considered to have caused a rejuvenation of the fluvial network. Peak disequilibrium occurred at the upstream end of the channel work after its completion in 1967. Point A in Figure 4 denotes the location of this peak disturbance (AMD), represents maximum rates of degradation, and serves as a starting time (1967) for a space-for-time substitution. Incision upstream according to Line C and aggradation downstream according to Line B progress from this point in time and space.

Degradation for 10 to 15 years at sites just upstream of A reduces gradients to such an extent that the river can no longer transport the loads delivered from degrading reaches further upstream. These sites then experience secondary aggradation due to the overadjustment by degradation processes (D in

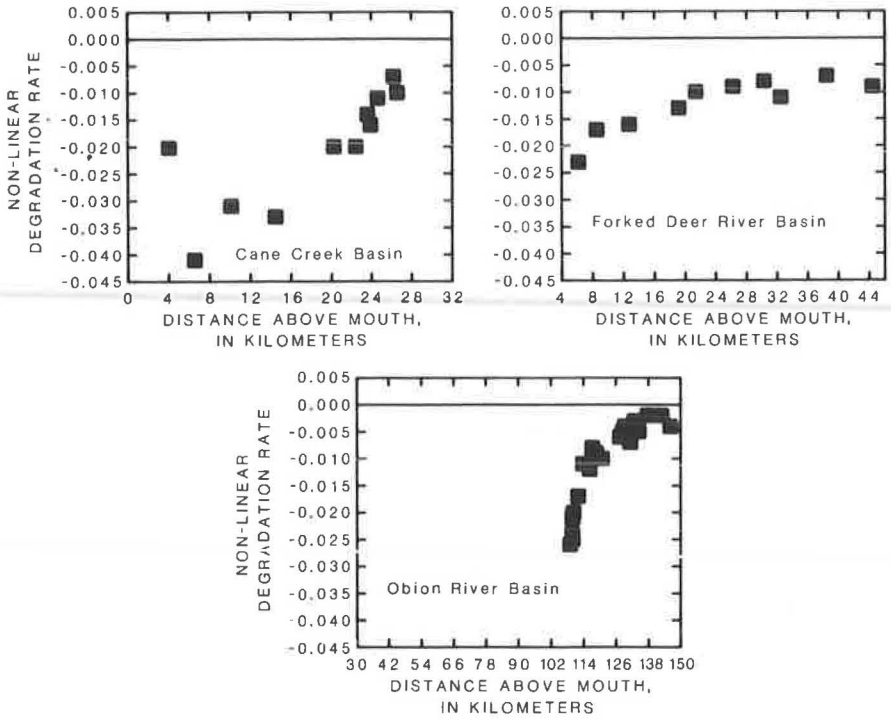

FIGURE 3 Longitudinal trends of degradation in three networks in western Tennessee.

Figure 4). This headward infilling occurs at magnitudes 78 percent less than the previous degradation rate, which suggests an overcompensation of 22 percent and oscillatory channel response. Expected shifts to secondary aggradation at sites further upstream that are presently degrading are provided by the inclusion of estimated data and serve to extend Line B-D in time and space. The bed level response model allows prediction of degradation and aggradation over time and space at any site along these river systems and is therefore extremely useful for the design of river-crossing structures.

Where Lines C and D approach the 0.00 line, gradation due to downstream modifications is minimized, and these sites will

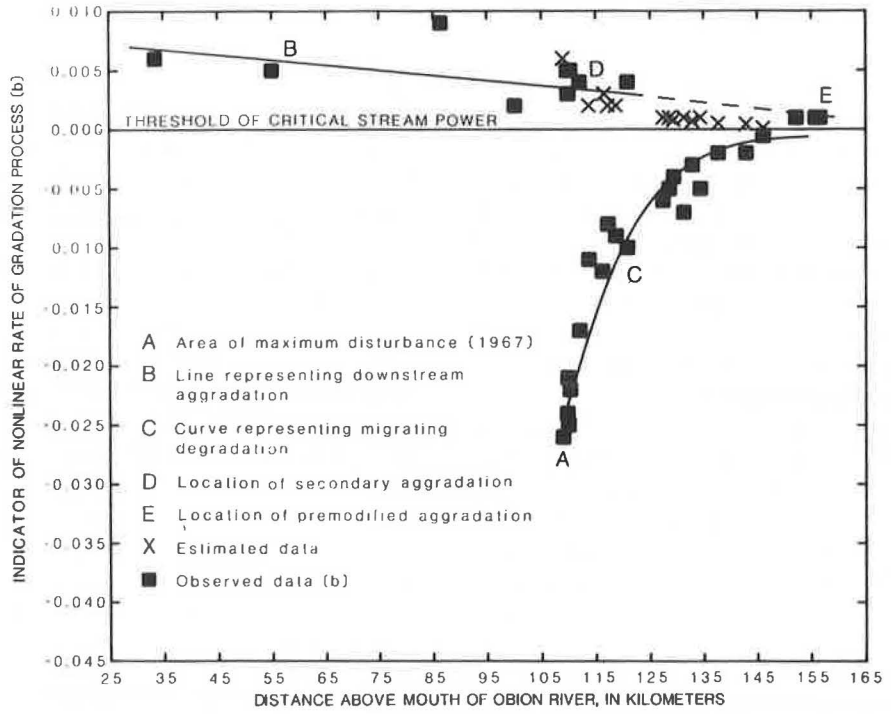

FIGURE 4 Model of bed level response for the Obion River system.

not degrade. This is estimated to take place near river kilometer 145 in the Obion River system. Upstream of the estimated intersection of the 0.00 line at E, aggradation continues to take place at low, premodified rates, according to "natural" basin and channel characteristics. Channel conditions far upstream of the AMD near E represent not only moderate adjustment processes and premodified aggradation rates but also conditions that will be attained by downstream reaches in the future as the channel network approaches quasi-equilibrium.

WIDTH ADJUSTMENT AND BANK SLOPE DEVELOPMENT

Channel widening (DW) and bank failure by mass-wasting processes are common attributes of adjusting channels in western Tennessee. Bank failure is induced by the overheightening and oversteepening of the bank by degradation and by undercutting at the toe of the bank *(9)*. Piping in the loess-derived bank materials enhances bank failure by internally destabilizing the bank.

The effect on channel widening of bed level lowering by degradation is reflected by the following direct correlation between the degradation exponent ($-b$) and DW where $r^2 = 0.50$, $S_L = 0.0001$, and $n = 49$. This relation implies that lower headward degradation rates reduce the tendency for channel widening upstream *(7)*. A summary of changes in channel width (DW) after the most recent major channel modifications of western Tennessee streams is given in Table 2. Mean DW-values for each stream are merely a point of reference and not a precise average of width adjustment because of the variability of gradation processes and the relative location of sites along a given stream. Minimum and maximum values of DW, however, do reflect a realistic range of width changes along the stream lengths studied.

PROCESSES AND STAGES OF BANK RETREAT AND SLOPE DEVELOPMENT

The processes and successive forms of bank retreat and bank slope development reflect the interaction of hillslope and fluvial processes. Interpretations of these processes and forms are based largely on bed level adjustment trends and botanical evidence *(7)*. An idealized representation of six stages of bank retreat and bank slope development is shown in Figure 5. The stages represent distinguishable bank morphologies that are characteristic of the various types of sites that describe bed level adjustment (Table 3).

Premodified Stage

Premodified bank conditions are assumed to be the result of "natural" land use practices and fluvial processes. Bank failure by mass wasting generally does not occur, and banks are considered stable. Premodified bank conditions (Stage I in Figure 5) are generally characterized by low-angle slopes (20 to 30 degrees), convex upper bank and concave lower bank shapes, and established woody vegetation along the top bank and downslope toward the low-flow channel. Stage I channel widths may narrow slowly with time as a result of mild aggradation and bank accretion. Sand often is found deposited on bank surfaces. Limited channel widening caused by bank caving and fluvial erosion may occur on some outside meander bends.

Constructed Stage

Construction of a new channel involves reshaping the existing channel banks or repositioning the entire channel. In either case, the banks are generally steepened, heightened, and made linear (Stage II in Figure 5). Modified western Tennessee channels generally are constructed as trapezoids with bank slopes ranging from 18 to 34 degrees. Channel widths are increased and vegetation is removed so that greater discharges can be conveyed within the channel banks.

Degradation Stage

The degradation stage (Stage III in Figure 5) is characterized by the lowering of the channel bed and the consequent increase in bank heights. Downcutting generally does not steepen bank slopes directly but maintains bank angles close to the angle of internal friction *(5, 10, 11)*. Steepening occurs when moderate flows attack basal surfaces and remove toe material along

TABLE 2 RANGE OF CHANGES IN CHANNEL TOP WIDTH (DW) BY STREAM

	DW, in meters					Years since most recent major channelization (from 1983)
	Mean	n	S	Min	Max	
Cane Creek	18.2	6	6.2	14	25	13
Cub Creek	2.1	4	5.1	0	6.7	13
Hoosier Creek	14.2	3	21.2	7.0	27	16
Hyde Creek	3.1	3	5.0	.3	5.4	18
Meridian Creek	3.4	2	3.0	2.4	4.3	16
North Fork Forked Deer River	10.3	4	16.9	3.0	25	10
North Fork Obion River	10.4	5	15.4	.6	25	16
Obion River	37.8	4	26.8	20	59	17
Pond Creek	2.9	3	1.7	2.1	4.3	5
Porters Creek	7.7	3	7.5	3.7	12	11
Rutherford Fork Obion River	7.2	5	11.4	0	18	14
South Fork Forked Deer River	13.6	6	11.5	4.9	27	14
South Fork Obion River	11.9	6	14.5	0	36	14

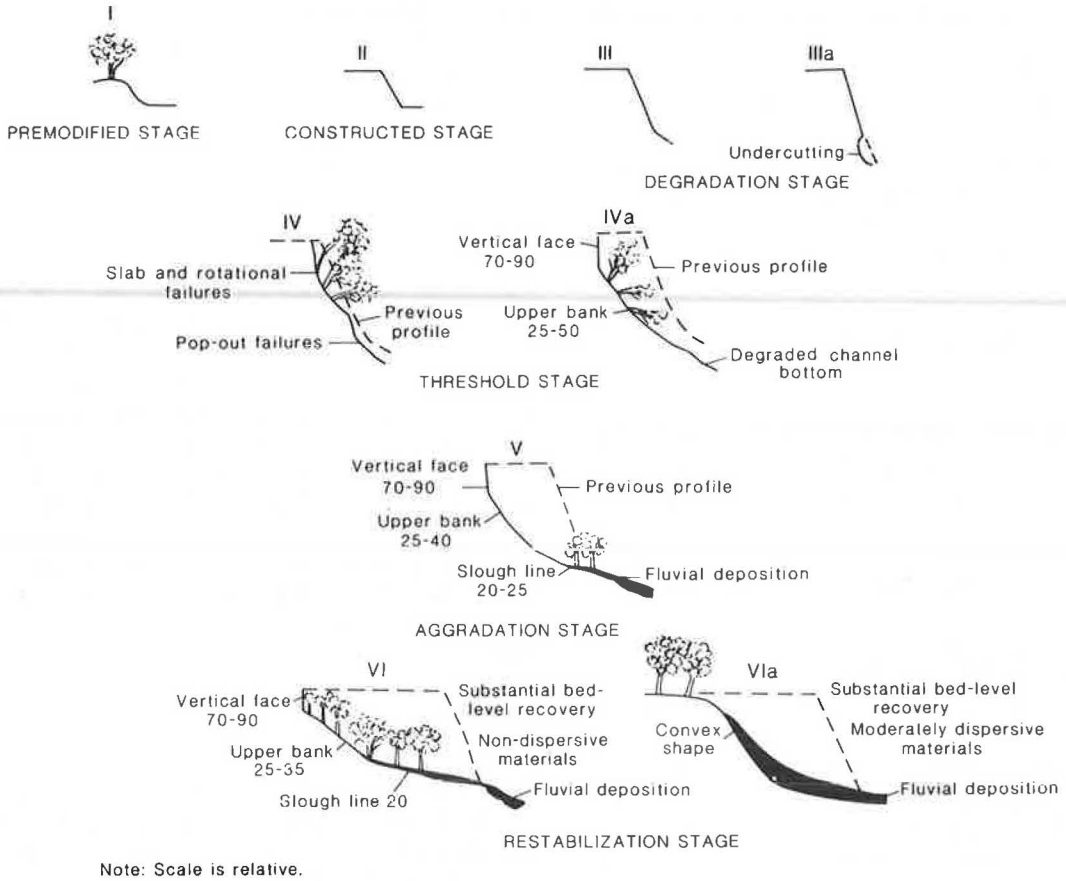

Note: Scale is relative.

FIGURE 5 Six stages of bank slope development.

the heightened banks (Stage IIIa in Figure 5). Ideally, widening by mass wasting does not occur because the critical bank height has not yet been exceeded. The degradation stage ends when the critical height of the material is reached.

Threshold Stage

Stage IV (Figure 5) is the result of continued degradation and basal erosion that further heighten and steepen the channel banks. The critical bank height is exceeded, and bank slopes and shapes become the product of mass-wasting processes. Slab failures occur as a result of excessive undercutting and loss of support for the upper part of the bank. Pop-out failures at the base of the bank caused by saturation and pore water pressure *(9)* similarly oversteepen the upper part of the bank. Deep-seated rotational failures shear along a circular arc and often become detached from the top bank surface by piping and tension cracking. These failures can leave 1.8- to 3-m-long

TABLE 3 STAGES OF BANK SLOPE DEVELOPMENT

Stage No.	Stage Name	Bed Level Adjustment Type	Location in Network	Process on Channel Bed	Active Widening	Failure Types	Bank Surfaces Present	Approximate Bank Angles (degrees)
I	Premodified	Premodified	Upstream-most reaches	Transport of sediment or mild aggradation	No	N/A	N/A	20–30
II	Constructed	N/A	Where applicable	Dredging	By man	N/A	N/A	18–34
III	Degradation	Migrating degradation	Upstream from AMD	Degradation	No	N/A	N/A	20–30
IV	Threshold	Migrating degradation	Close to AMD	Degradation	Yes	Slab rotational pop-out	Vertical face Upper bank	70–90 25–50
V	Aggradation	Secondary aggradation	Upstream of AMD	Aggradation	Yes	Slab rotational pop-out, low-angle slides	Vertical face Upper bank Slough line	70–90 25–40 20–25
VI	Restabilization	Downstream-imposed aggradation	Downstream of AMD	Aggradation	No	Low-angle slides, pop-out	Vertical face Upper bank Slough line	70–90 25–35 15–20

NOTE: AMD = area of maximum disturbance.

slickensides along the failure plane and have been observed to be as much as 60 m long and 6 m wide *(5)*. The bank also can fail as plates along a series of pipes that form in the bank mass and intersect the flood plain surface *(7)*. Occasional debris avalanching occurs as well. These failure mechanisms are most intense in highly dispersive loess materials, such as are found in the Cane Creek basin.

The failed material that comes to rest on the bank forms a definable surface at slopes ranging from 25 to 50 degrees (Stage IV in Figure 5). This surface is termed the "upper bank" *(5)* and can often be identified on field inspection by tilted and fallen vegetation. The "vertical face," representing the top section of the major failure plane, is developed concurrently. The vertical face may range from 70 to 90 degrees and represents the primary location of top bank retreat.

The threshold stage is the first of two that are dominated by active channel widening. Failed material may be carried off by moderate to high flows, thereby retaining the overheightened and oversteepened bank profile and giving the banks a scalloped appearance.

Aggradation Stage

Stage V (Figure 5) is marked by the onset of aggradation on the channel bed and often can be identified by deposited sand on bank surfaces. Bank retreat dominates the vertical face and upper bank sections because bank heights still exceed the critical height of the material. The failed material on the upper bank is subject to low-angle slides resulting from continued wetting of the material by rises in stage. This process flattens and extends the upper bank downslope. Older masses of failed material on the upper bank also move downslope by low-angle slides. Such masses show evidence of fluvial reworking and deposition low on the upper bank and create a low-angle surface (20 to 25 degrees) termed the "slough line," extending downslope from the upper bank *(5, 6)*. Reestablishment of woody vegetation on the slough line has been used to date renewed bank stability along several streams *(6)*.

A slow and prolonged period of bed level recovery (as with the loess bed channels) maintains bank heights greater than the critical height of the material for extended periods. Dispersion and tension cracking continue to weaken the vertical face. Parallel bank retreat along the vertical face, and flattening of the upper bank and slough line, may continue as the channel creates a new flood plain at an elevation lower than the previous one. The previous flood plain would then become a fluvial remnant, or terrace, over geologic time. This scenario of flood plain development is probably appropriate only for the most highly disturbed channels that are cut through deposits of dispersive loess, such as Cane Creek *(5)*. Stage V would then represent the final stage of bank slope development for these types of channels.

Restabilization Stage

The restabilization stage is marked by significant reduction of bank heights by aggradation on the channel bed and by fluvial deposition on the upper bank and slough line surfaces. Bank retreat along the vertical face by intense mass-wasting processes subsides because of lack of bank height relative to the critical height.

Cohesive banks along Porters and Cub creeks, and areas of the Obion River system that are composed of strongly nondispersive materials, can maintain a vertical face even though the surface is frequently wet by rises in stage. Woody vegetation extends to the base of the vertical face in these cases, and the old flood plain surface becomes a terrace (Stage VI, Figure 5). In channels the bank materials of which are only moderately dispersive and the bed level of which has sufficiently recovered to cause greater flow frequencies on the vertical face, the uppermost section of the bank may take a convex shape due to fluvial reworking and deposition (Stage VI, Figure 5). In some extensively aggrading downstream reaches, such as along the Obion River main stem, the flood plain surface maintains its role as a conduit for moderately high flows, and woody vegetation becomes reestablished at the top of the bank and on the flood plain surface *(6)*.

The six stages of bank slope development represent a conceptual model of width adjustment. Stages are induced by a succession of interactions between gradation and hillslope processes (Table 3). The model does not imply that each adjusting reach will undergo all six stages during the course of adjustment but that specific trends of bed level response result in a series of mass-wasting processes and definable bank forms. The conceptual framework of the simultaneous retreat of the vertical face, and flattening along surfaces below it, is supported by the observation of other investigators reported by Carson and Kirkby (*11*, p. 184).

CONCLUSIONS

Channel dredging and straightening between 1959 and 1972 in western Tennessee caused a series of morphologic changes along modified and adjacent reaches and tributaries. Simple power equations accurately describe bed degradation and aggradation over time. Degradation occurs for 10 to 15 years at sites upstream of the AMD and can lower bed level by as much as 6.1 m. Aggradation downstream of the AMD can reach 0.12 m/year with the greatest rates near the mouth. Distance upstream or downstream from the AMD is a principal independent variable in determining trends of bed level response. Initially degraded sites experience a secondary aggradation phase in response to excessive incisement and gradient reduction.

Adjustment of channel width is characterized by six stages of bank slope development: premodified, constructed, degradation, threshold, aggradation, and restabilization. Characteristic forms and processes of the six stages can be extrapolated to other river systems to ascertain the relative stability of an alluvial channel. Downcutting and toe removal during the degradation stage cause bank failure by mass-wasting processes when the critical height of the bank material is reached (threshold stage). Top bank widening continues through the aggradation stage as the slough line develops as an initial site of lower bank stability. The development of the bank profile is defined in terms of three dynamic surfaces: (*a*) vertical face (70 to 90 degrees), (*b*) upper bank (25 to 50 degrees), and (*c*) slough line (20 to 25 degrees).

REFERENCES

1. E. W. Lane. The Importance of Fluvial Morphology in Hydraulic Engineering. *Proceedings*, ASCE, Vol. 81, No. 795, 1955, 17 pp.
2. *Obion–Forked Deer River Basin, Tennessee.* Summary Final Report. Soil Conservation Service, U.S. Department of Agriculture, 1980, 43 pp.
3. C. H. Robbins and A. Simon. *Man-Induced Channel Adjustment in Tennessee Streams*. Water-Resources Investigations Report 82-4098. U.S. Geological Survey, 1983, 129 pp.
4. T. Blench. Factors Controlling Size, Form and Slope of Stream Channels. In *Fluvial Processes and Sedimentation*, 9th Hydrology Symposium, Edmonton, Alberta, Canada, 1973, pp. 421–439.
5. A. Simon and C. R. Hupp. Channel Widening Characteristics and Bank Slope Development Along a Reach of Cane Creek, West Tennessee. Water-Supply Paper 2290. In *Selected Papers in the Hydrologic Sciences* (S. Subitsky, ed.), U.S. Geological Survey, forthcoming.
6. C. R. Hupp and A. Simon. Vegetation and Bank-Slope Development. *Proc., 4th Federal Interagency Sedimentation Conference*, Vol. 2, 1986, pp. 55-83–5-92.
7. A. Simon. *Gradation Processes and Channel Evolution in Modified West Tennessee Streams: Process, Response, and Form.* Professional Paper. U.S. Geological Survey, forthcoming.
8. W. B. Bull. Threshold of Critical Power in Streams. *Geological Society of America Bulletin*, Part 1, Vol. 90, 1979, pp. 453–464.
9. C. R. Thorne, J. B. Murphey, and W. C. Little. *Stream Channel Stability*. Sedimentation Laboratory, U.S. Department of Agriculture, Oxford, Miss., 1981, 257 pp., Appendix D: Bank Stability and Bank Material Properties in the Bluffline Streams of Northwest Mississippi.
10. A. W. Skempton. Soil Mechanics in Relation to Geology. *Proceedings*, Yorkshire Geological Society, Vol. 29, 1953, pp. 33–62.
11. M. A. Carson and M. J. Kirkby. *Hillslope Form and Process.* Cambridge University Press, London, England, 1972, 475 pp.

Internal Energy Dissipators for Culverts on Steep Slopes with Inlet Control

A. L. SIMON, S. SARIKELLE, AND S. F. KOROM

Results of a model study of internal energy dissipators for culverts on a steep slope and operating under inlet control are discussed. The shortest ring chamber design that effectively reduces the outlet velocity is provided. Ring chamber diameters are expressed as a function of the upstream Froude number. Spacing and dimensions of roughness elements are related to ring chamber diameter. The model results are compared with prototype performance and adjusted to improve their accuracy. Hydraulic design parameters that affect the operation of such culverts are discussed, and practical design procedures are given.

Because a culvert offers less resistance to flow than does a natural stream channel, water usually exits a culvert with greater velocity. This increase in velocity can cause excessive erosion or scour of the downstream channel and lead to structural failure of the highway embankment and the culvert itself. For low outlet velocities, lining the downstream channel with rocks offers sufficient protection against erosion and scour. Rock protection is not sufficient, however, for high outlet velocities. For example, the Ohio Department of Transportation's (ODOT's) design manual specifies that rock channel protection should not be used for outlet velocities greater than 20 ft/sec *(1)*. These higher velocities are often reduced by the formation of a hydraulic jump that produces an outlet flow of greater depth and lower velocity. The hydraulic jump is usually produced by an energy dissipator constructed at the outlet of the culvert; but, if the culvert is on a steep slope and under inlet control (i.e., a high-energy culvert), a hydraulic jump can be formed in the culvert itself. This allows the energy dissipator at the culvert's exit to be simplified or even eliminated.

Hydraulic jumps in culverts can be produced by placing rings (roughness elements) on the inside perimeter of the culvert near the outlet. This end section with rings in it is set on a milder slope than the rest of the culvert and is called a ring chamber. Summarized here are the results of an ODOT-sponsored study *(2)* undertaken to develop the hydraulic design parameters necessary to optimize the design of ring chambers that effectively reduce the outlet velocities of high-energy culverts by producing a hydraulic jump in the ring chamber.

Department of Civil Engineering, The University of Akron, Akron, Ohio 44325.

BACKGROUND

Development of Ring Chamber

The use of circular roughness elements in high-energy culverts was first studied by Wiggert and Erfle *(3)* and Wiggert et al. *(4)*. They placed circular rings inside the periphery of model culverts of constant slope. For the culvert to flow full at the location of the dissipators, four dissipators of two different heights were needed. A larger ring upstream created a hydraulic jump that was maintained by three smaller rings downstream. The upstream ring was approximately twice the height of the downstream rings and was spaced approximately twice as far from them as they were from each other. These findings led to sizing and locating the downstream rings as dictated by the following equations:

$$0.06 \leq K/D \leq 0.09 \quad (1)$$

and

$$L/D = 1.5 \quad (2)$$

where

K = the height of the dissipators (ft),
D = the inside diameter of the culvert (ft), and
L = the spacing between the three smaller rings (ft).

Wiggert et al. also found that by maintaining a free surface throughout the length of a culvert with rings in it, a greater velocity reduction could be achieved than under full-flow conditions. This introduced the telescoping ring chamber in which the main section (inlet section) of the culvert is governed by the conventional design parameters and the ring chamber is sized by the following equation:

$$(Q^2/0.10g)^{1/5} < D_o < (Q^2/0.044g)^{1/5} \quad (3)$$

where

Q = the design flow (ft^3/sec),
g = the acceleration due to gravity (ft^3/sec), and
D_o = the inside diameter of the ring chamber (ft).

Equation 3 requires five rings sized and spaced according to

$$0.10 \leq K/D_o \leq 0.15 \quad (4)$$

and

$$1.5 \leq L/D_o \leq 2.5 \quad (5)$$

This free-surface design produced a tumbling flow characterized by acceleration between rings and a hydraulic jump over each ring. This produced velocity reductions ranging from 50 to 70 percent.

ODOT designed their first ring chamber for a high-energy culvert in 1974 using the equations for free-surface flow. The culvert and ring chamber were placed on a 4.4 percent slope. Pettit *(5)* suggested the need to reduce the slope of the ring chamber to 0.5 percent and add a settling distance beyond the last ring station. The steep 4.4 percent slope established a vertical velocity component that produced a scour hole at the outlet of the ring chamber. The settling distance allows the flow held back by the last dissipator to tumble to a lesser depth within the confines of the culvert. All subsequent ODOT high-energy culvert designs have ring chambers set at a slope of 0.5 percent or less.

ODOT also modified the shape of the dissipators from a solid ring to two ring segments (Figure 1). If water trapped in front of the solid rings froze, it could damage the joint between the dissipators and the inner wall of the ring chamber. The gap (G) was added at the bottom to allow for complete drainage. Removal of a section of the ring at the top promotes free-surface flow throughout the culvert. The upstream edge of the rings also had a 30-degree bevel added to aid in passing debris (Figure 2). All of these changes were substantiated in laboratory and field tests by Simon and Sarikelle *(6)*.

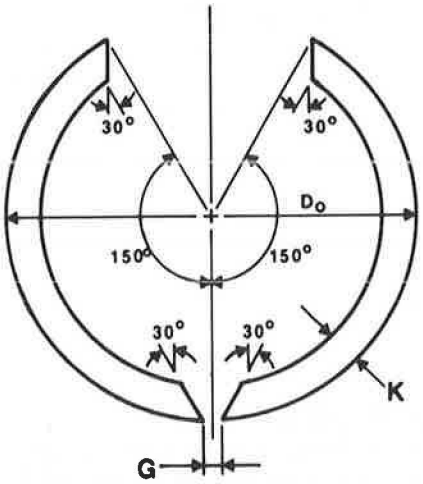

FIGURE 1 Modified two-piece dissipator.

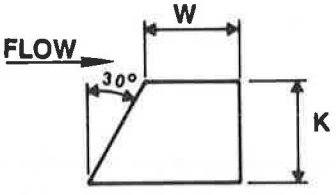

FIGURE 2 Cross section of ODOT dissipators.

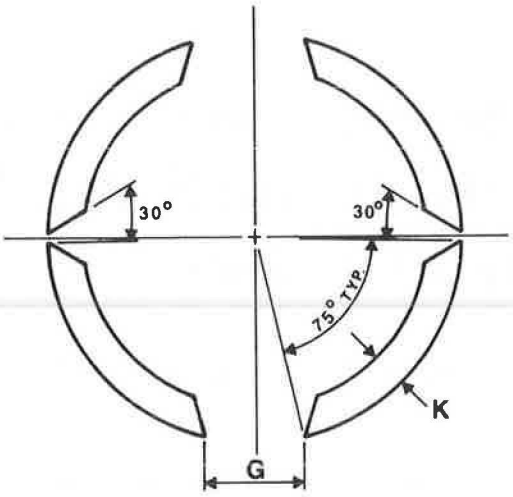

FIGURE 3 Four-piece dissipator.

ODOT later modified the ring dissipators from a two-piece to a four-piece design to simplify their installation in the ring chamber (Figure 3).

Froude Numbers Used in the Study

Because the dominant forces in open channel problems are controlled by gravity, viscous and other effects can be neglected and Froude modeling law will apply. This means that the ratio of gravitational forces to inertial forces will be the same in both model and prototype to maintain dynamic similarity. The Froude number is given by

$$F = V/(gL')^{1/2} \quad (6)$$

where V is the velocity of the flow and L' is a characteristic length, which for open-channel flow is the hydraulic depth. This value is defined as the area of flow normal to the flow's direction divided by the top width of the free surface. For rectangular channels this is simply the depth of flow. For circular channels, hydraulic depth computations are more complex. To simplify Froude number computations for circular channels in this study the hydraulic depth has been replaced by the actual depth.

Alternately, the true Froude number for a circular channel flowing less than half full can be approximated using

$$F' = 1.135F^{1.019} \quad (7)$$

where F' is the true Froude number computed using the hydraulic depth and F is the Froude number computed using the actual depth.

EXPERIMENTAL PROCEDURE

Models of culverts similar to the one shown in Figure 4 were assembled of clear acrylic in an adjustable-slope flume so that

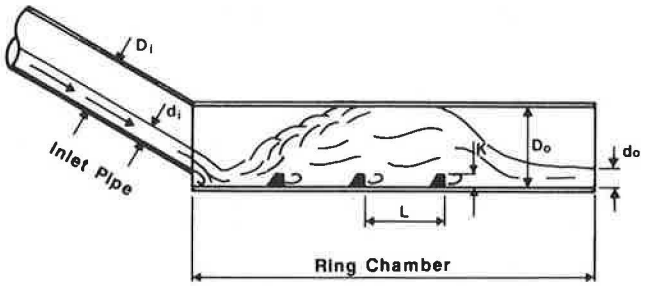

FIGURE 4 Ring chamber flowing just full.

ring dissipators of various numbers, types, and heights (K) could be used, distances between dissipators (L) could be varied, and the slope of the inlet pipe could be changed.

The ring chamber had an inside diameter (D_o) of 6.0 in. Four inlet pipes were used with inside diameters (D_i) of 4.0, 4.75, 5.5, and 6.0 in. This gave ring chamber-to-inlet size ratios (D_o/D_i) of 1.50, 1.26, 1.09, and 1.00, respectively.

Ring dissipators were molded to model the four-piece design shown in Figure 3 and a new two-piece design shown in Figure 5. This new design is the same as the four-piece design with the top two ring segments eliminated. It was believed that only the two bottom segments were necessary to produce a hydraulic jump in the ring chamber. Both designs were molded with dissipator heights (K) of 0.50, 0.75, and 1.00 in. to give relative heights (K/D) of 1/12, 1/8, and 1/6, respectively.

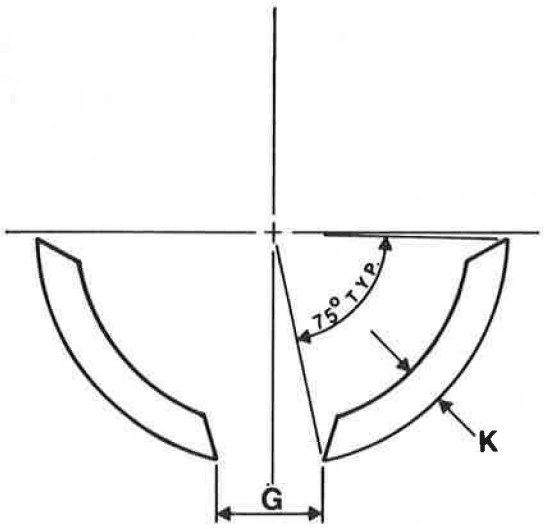

FIGURE 5 Improved two-piece dissipator.

Holes were drilled in the inlet pipes and ring chamber so flow depths could be measured with a point gauge. When these depths and the amount of flow (Q) from a calibrated flowmeter are known, the velocities can be computed.

Tests were run to find the minimum number of dissipators, the type of dissipators, the minimum relative height of dissipators (K/D_o), and the minimum relative spacing between dissipators (L/D_o) that produced a hydraulic jump in the ring chamber. It was found that four two-piece dissipators (as in Figure 5) with K/D_o of 1/8 and L/D_o of 1.0 produced one minimum design. Another was three two-piece dissipators with K/D_o of 1/6 and L/D_o of 1.0. Other designs worked as well but required longer ring chambers or larger ring chamber diameters for a given inlet pipe size and design flow.

To test the design of four two-piece dissipators with K/D_o of 1/8 and L/D_o of 1.0, the inlet pipe was placed on a slope of approximately 2 to 1. The discharge was increased until the ring chamber flowed just full (Figure 4), and the inlet and outlet flow depths were measured (d_i and d_o, respectively). The inlet flow depth was measured one ring chamber distance from the end of the inlet pipe. Next, the discharge was increased until a full-flow condition developed in the inlet pipe to a one ring chamber diameter distance into the pipe (Figure 6). (This was not done for D_0/D_i = 1.50). This is called a choked condition. The values for d_i and d_o were measured again. These steps were repeated for decreasing values of the inlet pipe's slope. The procedure was followed for each of four inlet pipe diameters: 4.00, 4.75, 5.5, and 6.00 in.

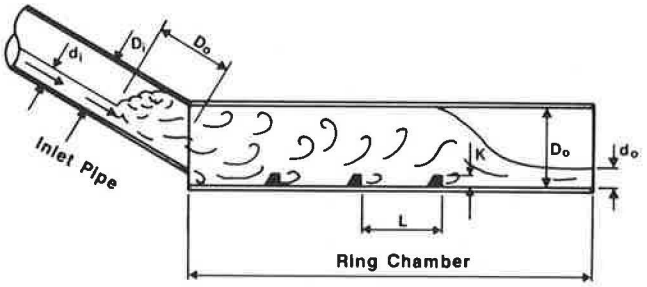

FIGURE 6 Ring chamber flowing fully choked.

To test the design of three two-piece dissipators with K/D_o of 1/6 and L/D_o of 1.0, the procedure was repeated, but measurements were taken only for choked conditions.

All of the tests were carried out with the ring chamber set at a slope of 0.5 percent.

DISCUSSION OF RESULTS

This section has two parts. In the first are discussed the results shown in Figures 7–10, which represent the results obtained from the model studies. The second part covers two studies comparing the energy reduction performance of models and

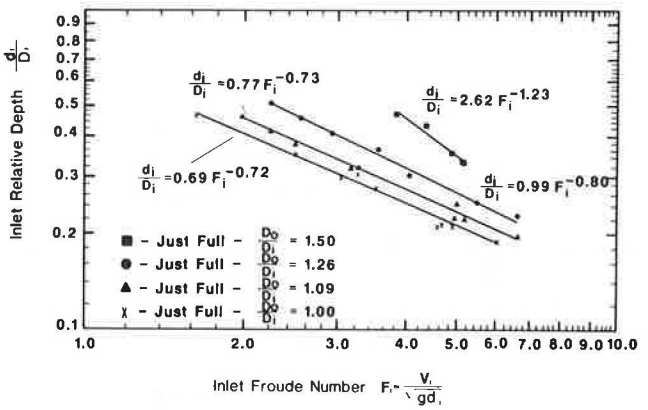

FIGURE 7 Performance graph for just-full conditions: four dissipators (K/D_o = 1/8, L/D_o = 1.0).

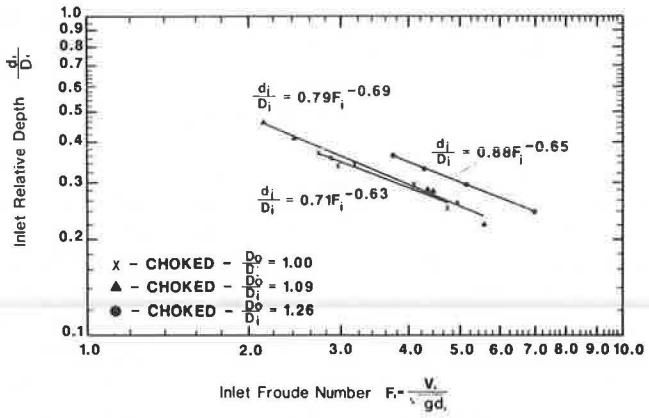

FIGURE 8 Performance graph for choked conditions: four dissipators (K/D_o = 1/8, L/D_o = 1.0).

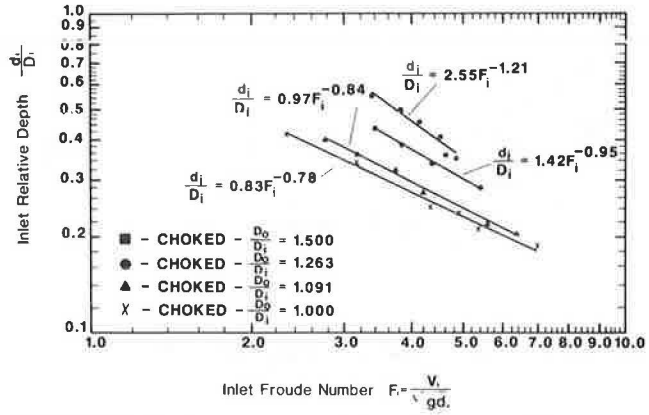

FIGURE 9 Performance graph for choked conditions: three dissipators (K/D_o = 1/6, L/D_o = 1.0).

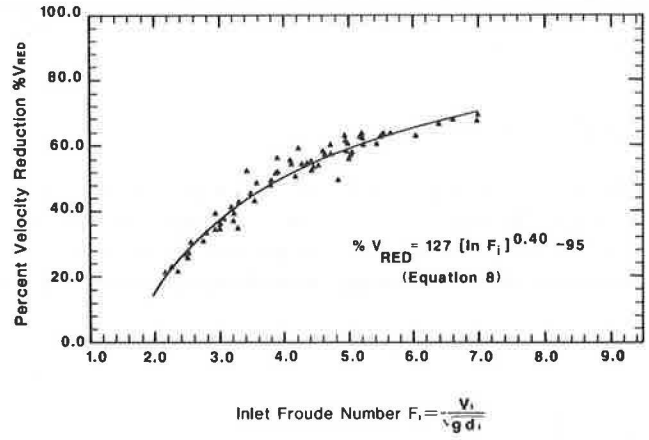

FIGURE 10 Best-fit curve for percent velocity reduction.

prototypes of high-energy culverts with ring chambers. This information is used to calibrate the velocity reduction curve shown in Figure 10, which can be used to predict velocity reductions in prototype applications.

Graphic Presentation of Results

Figures 7–9 show the inlet Froude number (F_i) and the inlet relative depth (d_i/D_i) necessary to cause certain flow conditions in the ring chamber. For instance, in Figure 7 the bottom line represents the best fit through data points taken from tests of four two-piece dissipators where K/D_o = 1/8, L/D_o = 1.0, the ring chamber diameter was the same as the inlet pipe diameter (D_o/D_i = 1.00), and the culvert was flowing just full. Points on this line give the inlet Froude number and inlet relative depth necessary to cause the given ring chamber to flow just full (Figure 4). Points below this line indicate less than full flow condition for the given Froude number and inlet relative depth. Similarly, any point above this line indicates a pressurized flow condition for the Froude number and inlet relative depth given.

The next line gives the inlet Froude numbers and inlet relative depths for just-full conditions when the ring chamber diameter is 1.09 times larger than the inlet pipe diameter.

The difference between Figures 7 and 8 is that the latter represents choked conditions (Figure 6).

Figure 9 is also for choked conditions but with a shorter ring chamber with fewer but larger dissipators (i.e., three two-piece dissipators with K/D_o = 1/6 and L/D_o = 1.0).

Figure 10 shows percent velocity reduction ($\%V_{RED}$) as a function of F_i. Inlet relative depth values from all three sets of tests are represented. The best-fit equation for percent velocity reduction is

$$\%V_{RED} = 127\ [\ln(F_i)]^{0.40} - 95 \quad (8)$$

where $\ln(F_i)$ indicates the natural logarithm of the inlet Froude number.

The limited amount of scatter about the best-fit curve shown in Figure 10 suggests that all of the ring chamber designs tested caused about the same velocity reduction for a given inlet Froude number. This implies that the hydraulic jump causes the velocity reduction (i.e., the design of the ring chamber that produces the jump is relatively insignificant). Thus the ring chamber design that produces hydraulic jumps and is most economical to construct may be selected without limiting velocity-reducing capacity.

A similar figure showing percent energy reduction ($\%E_{RED}$) as a function of f_i could also be drawn. The best-fit equation for percent energy reduction for all tests is

$$\%E_{RED} = 160\ [\ln(F_i)]^{0.35} - 115 \quad (9)$$

Prototype Ring Chamber Tests and Calibration of Velocity Reduction Curve

Wiggert et al. *(4)* compare energy reductions in a 6-in.-diameter model and an 18-in.-diameter concrete prototype. Simon and Sarikelle *(6)* compare results for a model with a 4.06-in. inlet and a 5.69-in. ring chamber with those for a concrete prototype with a 60-in. inlet and an 84-in. ring chamber. Both sets of results are given in Table 1.

The differences in energy reductions between the models and prototypes are mainly due to viscous shear forces. Although these forces are not as significant as gravitational forces, in open-channel flow they affect the results. Viscous effects in prototype scale are not necessarily the same as those in the corresponding models that were built according to Froude's law. Comparison of model and field studies has shown that viscous forces affect the flow more in a smaller-diameter pipe than in a larger-diameter pipe. Energy losses in the smaller models should be greater than energy losses in the

TABLE 1 COMPARISON OF MODEL AND PROTOTYPE ENERGY REDUCTIONS

Model Diameter, D_O (in.)	Prototype Diameter, D_O (in.)	Model Energy Reduction (%)	Prototype Energy Reduction (%)	Difference in Energy Reduction (%)
6	18	87.2	65.0	25.5
6	18	83.6	53.0	36.6
6	84	90.0[a]	55.8	38.0
6	84	90.0[a]	60.2	33.1

[a]Estimated value based on results in Simon and Sarikelle *(6)*.

larger prototypes. These results are given in Table 1. The values in the last column of this table show that the energy-reducing performance of the prototypes is approximately one-third less than predicted by the models. This rather significant difference may be explained by the fundamental laws of hydraulic modeling. Expressing the ratio of viscous forces per unit discharge, it is found that it equals the square root of the length ratio of the model to the prototype *(7)*. Consequently, a culvert that is nine times larger than the model would have one-third of the viscous force per unit discharge of the model. Because energy losses are proportional to the viscous shear in the fluid, it is explainable that there is relatively more energy lost per unit volume flowing in the model. For this reason, the energy reduction equation for the models in this study (Equation 9) can be reduced one-third. It becomes

$$\%E_{RED} = 107\ [\ln(F_i)]^{0.35} - 77 \tag{10}$$

Computations show that if the energy reduction equation is reduced by one-third, the velocity reduction equation should also be reduced. But the amount of this reduction varies depending on the inlet pipe's flow conditions (F_i and d_i/D_i). Because of this and in recognition of the limited amount of prototype performance data available for this study, it is recommended that the velocity reduction equation also be reduced one-third. It becomes

$$\%V_{RED} = 85\ [\ln(F_i)]^{0.40} - 63 \tag{11}$$

Figure 11 shows a plot of Equation 11. It should only be used for culverts 18 in. or larger in diameter.

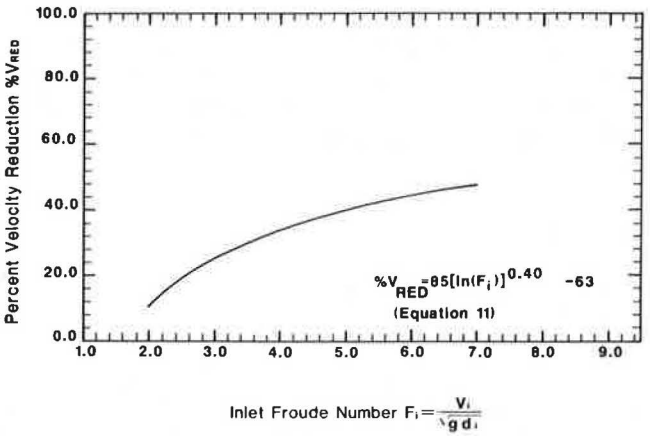

FIGURE 11 Calibrated percent velocity reduction curve for prototypes.

CONCLUSIONS

Close inspection of the results shown in Figures 7–9 reveals that of the three sets of tests the two for choked conditions allow for higher Froude numbers and inlet relative depths for a given D_o/D_i-value. Therefore the design flow can be greater for given diameters of the inlet and ring chamber if the ring chamber is designed to flow fully choked rather than just full. There is not a large difference between the results for the two sets with choked conditions so it is better to use the ring chamber design that would be less expensive to construct. Therefore the design with three two-piece dissipators (Figure 5) with $K/D_o = 1/6$ and $L/D_o = 1.0$ should be chosen over the design with four two-piece dissipators with $K/D_o = 1/8$ and $L/D_o = 1.0$ because it allows for a shorter ring chamber. This design follows the data shown in Figure 9.

Figure 12 is a reproduction of Figure 9 that may be used as a design aid for determining choked-flow conditions in ring chambers of various sizes. Designs with inlet relative depths and inlet Froude numbers that fall on or below the appropriate values are acceptable.

Other hydraulic design parameters that affect the operation of a ring chamber are discussed next.

Slope

Results shown in Figures 7–9 were obtained with the ring chamber set at a 0.5 percent slope. Slight variations from this slope did not affect the performance of the ring chamber. It is therefore recommended that the slope be kept in the range of 0.2 to 0.7 percent.

Distance to First Dissipator

The distance from the end of the inlet pipe to the first dissipator L_1) should be set at 1.33 D_o. If it is less than this value and the inlet pipe–ring chamber connection is built such that there is a drop from the invert of the inlet to the invert of the ring chamber, the flow could shoot over the first dissipator.

Drainage Gap

The drainage gap (G) between the two segments that make up each dissipator was sized by ODOT (Pettit, unpublished data) to be in the range:

$$1/13 \le G/D_o \le 1/6.5 \tag{12}$$

In this study, $G/D_o = 1/8$; therefore it is recommended that

$$1/13 \le G/D_o \le 1/8 \tag{13}$$

Dissipator Width

The dissipator width (W) is based on structural considerations. It should be wide enough to allow reinforcing bars to be placed in the dissipator segments to protect them from damage from collisions with passing debris. The dissipator widths given in Table 2 are those given by ODOT (Pettit, unpublished data).

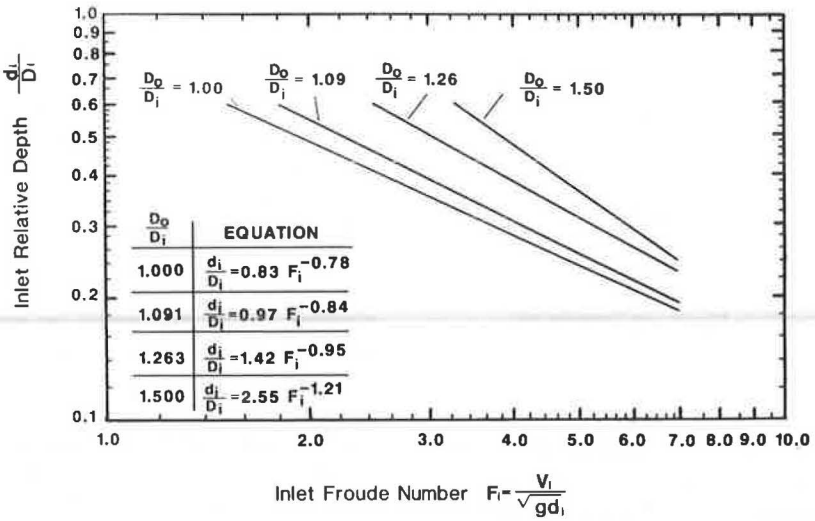

FIGURE 12 Design graph for ring chamber diameter sizes (D_o).

TABLE 2 RING CHAMBER DESIGN GUIDE

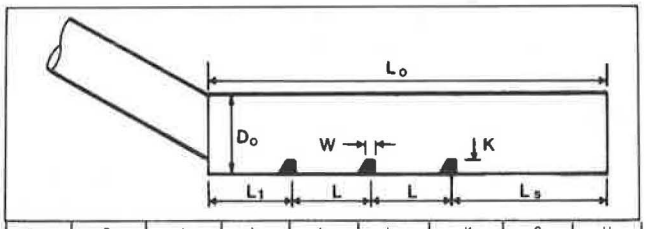

D_o (in.)	D_o (ft.)	L_1 (ft.)	L (ft.)	L_s (ft.)	L_o (ft.)	K (in.)	G (in.)	W (in.)
36	3	4	3	6	16	6	4	7
42	3-1/2	6	4-1/2	9	24	7	5	7
48	4	6	4-1/2	9	24	8	6	8
54	4-1/2	6	4-1/2	9	24	9	6	8
60	5	8	6	12	32	10	7	9
66	5-1/2	8	6	12	32	11	8	9
72	6	8	6	12	32	12	9	9
78	6-1/2	10	7-1/2	15	40	13	9	9
84	7	10	7-1/2	15	40	14	10	9
90	7-1/2	10	7-1/2	15	40	15	11	9
96	8	12	9	18	48	16	12	10
102	8-1/2	12	9	18	48	17	12	10
108	9	12	9	18	48	18	13	10
114	9-1/2	14	10-1/2	21	56	19	14	10
120	10	14	10-1/2	21	56	20	15	10
126	10-1/2	14	10-1/2	21	56	21	15	12
132	11	16	12	24	64	22	16	12
138	11-1/2	16	12	24	64	23	17	12
144	12	16	12	24	64	24	18	12
150	12-1/2	18	13-1/2	27	72	25	18	12
156	13	18	13-1/2	27	72	26	19	12
162	13-1/2	18	13-1/2	27	72	27	20	15
168	14	20	15	30	80	28	21	15
174	14-1/2	20	15	30	80	29	21	15
180	15	20	15	30	80	30	22	15

Settling Distance

The settling distance (L_s) is the distance from the last dissipator to the end of the ring chamber. In this region water obstructed by the last dissipator tumbles to a lesser depth. The settling distance should be long enough to contain this tumbling action so that it does not increase the erosion potential at the culvert's exit. This acceleration to a lesser depth is completed within a $2D_o$ distance after the last dissipator.

Tailwater Effects

The results in this study were obtained with no tailwater. If a prototype has tailwater sufficient to maintain subcritical flow, it will tend to further reduce the outlet velocity; however, it is noted that for most inlet-control conditions tailwater is not considered effective in reducing outlet velocities *(8)*. Excessive tailwater above the culvert outlet concentrates flow. Tailwater conditions also affect the geometry of the scour hole. The reader should check a study of this subject conducted by the U.S. Army Corps of Engineers *(9)*.

Venting

When a hydraulic jump is produced in the ring chamber it can cause a negative pressure in the inlet. This negative pressure can be eliminated by venting the pipe anywhere upstream of the hydraulic jump. It is known that venting causes the exit velocity to increase, but the amount of increase cannot be measured accurately because of air entrainment in the outlet flow.

If venting is desired, the diameter of the ring chamber should be increased to the next available pipe size over the one determined by the design procedure described hereafter. (Other hydraulic parameters should increase for the new D_o as in Table 2).

Design Procedure

The steps necessary to design a ring chamber based on the results of this study follow.

1. Find outlet velocity: The flow in most properly vented culverts on steep slopes reaches normal depth by the end of the culvert *(9)*. Compute the outlet velocity based on normal depth of the culvert without a ring chamber on it. This step can be

simplified by using information such as that given in Hydraulic Design Series 3 *(10)*.

If the computed velocity exceeds the maximum allowable for rock channel protection [20 ft/sec for ODOT *(1)*] and the culvert is on a steep slope and under inlet control, a ring chamber based on this study can be used to reduce outlet velocity.

2. Assume ring chamber diameter size (D_o): Assume a ring chamber–to–inlet ratio (D_o/d_i). To start with, choose a diameter of ring chamber from commercially available culvert sizes such that D_o/D_i is close to 1.25. The length of the ring chamber (L_o) is then obtained from Table 2.

3. Find new slope of inlet pipe: Find the new slope of the inlet pipe now that a ring chamber with a slope of from 0.2 to 0.7 percent is to be attached to it. This involves some simple trigonometry.

4. Find new inlet velocity and normal depth: Find, at the end of the inlet, the new velocity as in Step 1 and the normal depth, both with the new slope found in Step 3.

5. Check Figure 12: Find F_i at the end of the inlet using the normal depth from Step 4 and check Figure 12 to see if the assumed ring chamber size is correct. If it is not, repeat Steps 2 through 4 with increasingly larger or smaller ring chamber diameters until the results agree with Figure 12.

For D_o/D_i-values not represented by the equations on Figure 12, it is necessary to linearly interpolate between the two closest lines that are represented by equations. For instance, if $D_o/D_i = 1.4$, it is necessary to linearly interpolate between the lines for $D_o/D_i = 1.26$ and $D_o/D_i = 1.50$.

6. Find reduced outlet velocity: Find the reduced outlet velocity with Equation 11 or Figure 11. If the outlet velocity is still greater than the maximum allowable for rock channel protection, additional measures will be needed to reduce this velocity.

7. Check if venting is necessary: If venting is necessary, the diameter of the ring chamber should be increased to the next available size greater than that found in Step 5.

8. Find other hydraulic parameters: With the D_o found in Step 5 or 7, determine L_1, L, L_s, L_o (total length of ring chamber), K, G, and W from Table 2.

ACKNOWLEDGMENTS

The authors are indebted to the Ohio Department of Transportation for its continued support of their research on energy dissipation in culverts. The success of this study was greatly enhanced by the helpful advice of John D. Herl, John O. Hurd, C. Gene Pettit, and Leon O. Talbert of ODOT. Also, the cooperation of the FHWA, U.S. Department of Transportation, is gratefully acknowledged along with the helpful comments of Marvin I. Espeland and his staff at FHWA.

REFERENCES

1. *Location and Design Manual*. Ohio Department of Transportation, Columbus, Feb 1978, Section 1122.
2. A. L. Simon and S. Sarikelle. *Internal Energy Dissipators for Culverts*. Report FHWA/OH-84/007. Department of Civil Engineering, University of Akron, Akron, Ohio, Sept. 1984.
3. J. M. Wiggert and P. D. Erfle. Culvert Velocity Reduction by Internal Energy Dissipators. *Concrete Pipe News*, American Concrete Pipe Association, Arlington, Va., Oct. 1972, pp. 87–93.
4. J. M. Wiggert, P. D. Erfle, and H. M. Morris. Roughness Elements as Energy Dissipators of Free-Surface Flow in Circular Pipes. In *Highway Research Record 373*, HRB, National Research Council, Washington, D.C., 1971, pp. 64–73.
5. C. G. Pettit. The Enclosure of Permars Run. *Concrete Pipe News*, American Concrete Pipe Association, Arlington, Va. Feb. 1980, pp. 7–11.
6. A. L. Simon and S. Sarikelle. *Field and Laboratory Evaluation of Energy Dissipators for Culverts and Storm Drain Outlets*. Report Ohio DOT-03-79. Department of Civil Engineering, University of Akron, Akron, Ohio, Dec. 1980, Vol. 1, pp. 87–90.
7. A. L. Simon. *Hydraulics*, 3rd ed. John Wiley and Sons, New York, 1986.
8. Hydraulic Charts for the Selection of Highway Culverts. In *Hydraulic Engineering Circular 5*, Office of Engineering, FHWA, U.S. Department of Transportation, Dec. 1965, Chapter II, pp. 5–12.
9. Hydraulic Design of Energy Dissipators for Culverts and Channels. In *Hydraulic Engineering Circular 14*, Office of Engineering, FHWA, U.S. Department of Transportation, Nov. 1975, Chapters 3 and 5, pp. III-3 and V-1 to V-6.
10. *Design Charts for Open-Channel Flow*. Hydraulic Design Series 3. FHWA, U.S. Department of Transportation, March 1979.

Effects of Salts on Erosion Rate of Unsaturated Compacted Montmorillonite Clays

ALAEDDIN SHAIKH, JAMES F. RUFF, AND STEVEN R. ABT

Erosion rates of unsaturated compacted calcium montmorillonite and sodium montmorillonite clays were measured under a range of tractive shear stresses in a rectangular flume. The calcium montmorillonite was treated with calcium chloride and sodium carbonate to obtain samples with different chemical composition. Samples were compacted at nearly optimum water content under 700 Pa into sample containers with 160-cm^2 surface area and subjected to flowing water in the flume. The tractive stress on the bottom of the flume was determined by measuring the velocity distribution of the flow and using the Prandtl–von Karman equation. The tractive stress ranged from 1.67 to 12.9 Pa. The erosion rate of naturally occurring calcium montmorillonite was two orders of magnitude higher than that of sodium montmorillonite. When calcium montmorillonite was treated with 0.88 percent by dry weight sodium carbonate, the erosion rate was reduced to the same order as that of sodium montmorillonite. Addition of calcium chloride had no appreciable influence on the erosion rate of calcium montmorillonite. Empirical equations have been developed to estimate the erosion rate of compacted unsaturated montmorillonite clay as a function of sodium adsorption ratio and tractive stress.

Surface erosion by rainfall and flowing water can severely damage earth structures such as earth dams and highway embankments. These structures are often constructed from unsaturated compacted cohesive soils, and therefore an understanding of erodibility (relative susceptibility to erosion under an eroding force) of such soils is necessary for safe design of earth structures. Surface erosion can be caused by overtopping and by sheet or concentrated flow over embankments. The extent of erosion depends on the erosion resistance of the soil as well as the dynamics of the eroding flow. Certain soils in nature are highly erodible. Severe erosion damage to embankments in the form of deep gullies caused by rainfall has been reported by Sherard et al. *(1)*.

In recent years the results of extensive studies *(2–9)* have shown that pore water chemistry plays an important role in erosion resistance of saturated consolidated cohesive soils. The influence of pore water chemistry (or salt additives) on erosion resistance (or erosion rate) of unsaturated compacted cohesive soils has not been fully investigated. However, earth structures are compacted and usually are in an unsaturated state, especially the surface layer that is exposed to rainfall and flowing water. An unsaturated soil may slake as the result of water penetrating the soil and increasing the pore air pressure. In this case, the erosion mechanism will differ from that of saturated soils. Consequently, the relative contribution of salts to erosion rate also will differ for unsaturated and saturated soil.

Department of Civil Engineering, Colorado State University, Fort Collins, Colo. 80523.

The objectives of this paper are to describe the influence of sodium and calcium salts on the erosion rate of unsaturated compacted montmorillonite clays and to provide empirical relationships for estimating the erosion rate of such soils as a function of tractive stress and sodium adsorption ratio.

The information provided in this paper will help engineers to realize the influence of salts on the erosion rate of unsaturated compacted montmorillonite clays. The engineer will then select an appropriate soil for construction and maintenance of embankments or will stabilize the highly erodible soil with chemical treatment.

The empirical relationship can be used to evaluate the extent of erosion and the possibility of failure of an embankment by surface erosion.

EXPERIMENTAL INVESTIGATION

The materials and method of investigation are briefly described in this paper. Detailed descriptions are presented by Shaikh *(10)*.

Materials

Two commercially available montmorillonites, a sodium montmorillonite (No. 200 Volclay bentonite) and a calcium montmorillonite (Panther Creek southern bentonite), were selected for this study. An X-ray diffraction analysis showed that both clays are composed of well-crystallized montmorillonite mineral. The physical properties of these minerals are given in Table 1.

Chemical Treatment

Preliminary test results showed that the erosion rate of Ca-montmorillonite was about two orders of magnitude higher than that of Na-montmorillonite. The pore water chemistry was assumed to be the major cause of the difference in erosion rate. To verify this assumption, the Ca-montmorillonite was treated with calcium chloride and sodium carbonate. The pore water chemistry of the soil samples is characterized by sodium adsorption ratio [SAR = Na/0.5(Ca + Mg)] and total dissolved salts (TDS = Ca + Mg + Na + K) in a saturation extract. Treatment of Ca-montmorillonite with sodium salts may not

TABLE 1 PHYSICAL PROPERTIES OF SODIUM AND CALCIUM MONTMORILLONITES

	Na-Montmorillonite	Ca-Montmorillonite
Median size (μm)	< 0.1	4
Specific gravity	2.70	2.77
Liquid limit	522	90
Plastic limit	41	50
Plasticity index	481	40
Optimum water content[a] (%)	34	47
Optimum dry density[a] (g/cm^3)	1.20	1.07

[a] From standard Proctor test.

produce a mineral analogous to the Na-montmorillonite, but such treatment will reduce the erosion rate of the Ca-montmorillonite by two orders of magnitude, to the same order of magnitude as that of Na-montmorillonite.

For chemical treatment of the Ca-montmorillonite, the amount of the salt required to reach a specific value of SAR or TDS in the saturation extract was estimated and dissolved in distilled water. Pure Ca-montmorillonite was then sprayed with the desired amount of the salt solution and mixed with distilled water to form a slurry paste. The samples were then kept in watertight plastic bags for 2 weeks and intermixed every day of the first week; water was added, if necessary, to keep the samples soft if the samples became hard as the result of chemical reactions. The samples were air dried and thoroughly ground. The values of SAR and TDS of the treated samples were measured and are given in Table 2.

The term "pure Ca-montmorillonite" or "Ca-montmorillonite" will be used to indicate the Ca-montmorillonite at its natural composition. The treated samples of Ca-montmorillonite will be referred to as "Ca-montmorillonite + percentage salt." The concentration of soluble cations in a saturation extract, TDS, SAR, and some other physicochemical properties of the clay samples (with and without chemical additives) are given in Table 2.

Eroding Water

Tap water was used as eroding water, and each test was started with clean water. The quantity of total dissolved salts in the eroding water was less than 2.2 meq/L, and the pH of water was 7.7. The temperature of the eroding water was maintained at 18°C ± 1°C by adding hot or cold water during testing.

Sample Preparation

To compact the samples, the optimum water content of the clays was first determined by the standard Proctor test (values are given in Table 1). The air-dry samples were then sprayed with tap water to nearly optimum water content. For the first sample, an excess amount of wet soil was pressed into the sample container at 700 kPa pressure using a hydraulic press and a specially designed rectangular mold and piston. The surface of the sample was then trimmed flush with the top edges of the container. The wet weight of the remaining soil in the sample container was considered the "optimum wet weight." A sample containing material equal in weight to the optimum wet weight was pressed into the sample container until it produced a soil sample the surface of which was flush with the edges of the container. The rest of the samples were then prepared by pressing the optimum wet weight in the sample container until the surface of the sample was flush with the edges of the container. Compacted samples were stored in plastic bags for 24 hr before erosion testing.

Testing Apparatus and Procedures

Erosion tests were performed using a rectangular Plexiglas flume 15.5 cm wide, 11 cm deep, and 250 cm long with adjustable slope. A schematic drawing of the flume and sample containers is shown in Figure 1. The sample containers were 15.2 cm long, 10.5 cm wide, and 2.25 cm deep. The flume floor was modified so that the surface of the sample was flush with the bottom of the flume. Water was recirculated in the system. The depth of flow ranged from 0.8 to 2.1 cm. The flow rate was measured by a precalibrated Venturi meter, and uniformity of flow depth was maintained by an upstream control. The velocity profiles along the flume at sections shown in Figure 1 were measured using a Pitot tube 0.3 cm in outside diameter connected to a pressure transducer and readout system.

The tractive stress (τ) exerted on the flume bottom was estimated by measuring the velocity profiles and using the Prandtl–von Karman equation for smooth channels (*11*, pp. 168, 200),

TABLE 2 CHEMICAL PROPERTIES OF MONTMORILLONITE CLAY SAMPLES USED IN EXPERIMENTAL INVESTIGATION

			Concentration of Cations in Saturation Extract (meq/L)							Exchangeable Cations (meq/100 g)					
Clay	Paste pH	Conductance (mmhos/cm)	Ca	Mg	Na	K	TDS	SAR	% Sat.	Ca	Mg	Na	K	CEC	ESP
Na-montmorillonite	9.8	1.8	1.2	0.6	18.7		20.5	19.8	755.6	20.1	7.00	53.70	0.90	84.8	63.30
Ca-montmorillonite	8.2	0.7	5.9	1.2	0.7		7.8	0.4	96.6	70.9	8.10	0.46	1.00	82.8	0.56
Ca-montmorillonite + 0.80% $CaCl_2$			242.0	32.2	5.4	3.5	283.0	0.5	89.5	74.8	3.00	0.06	1.19	79.1	0.10
Ca-montmorillonite + 1.60% $CaCl_2$			374.0	39.9	6.9	4.6	425.0	0.5	93.5	83.0	2.90	0.14	1.24	87.3	0.20
Ca-montmorillonite + 0.22% Na_2CO_3			2.3	0.9	5.0	0.3	8.5	3.9	145.8	68.7	7.89	3.66	1.21	81.5	4.50
Ca-montmorillonite + 0.88% Na_2CO_3			0.8	0.5	9.3	0.1	10.7	11.4	208.5	53.3	7.75	21.63	1.18	84.0	25.80

NOTE: Ca, Mg, Na, K = calcium, magnesium, sodium, and potassium cations; TDS = total dissolved salts = Ca + Mg + Na + K; SAR = sodium adsorption ratio = $Na/[0.5(Ca + Mg)]^{1/2}$ in $(meq/L)^{1/2}$; % Sat. = percent saturation, water content of the paste used for saturation extract; CEC = cation exchange capacity; and ESP = exchangeable sodium percentage, 100 Na/CEC.

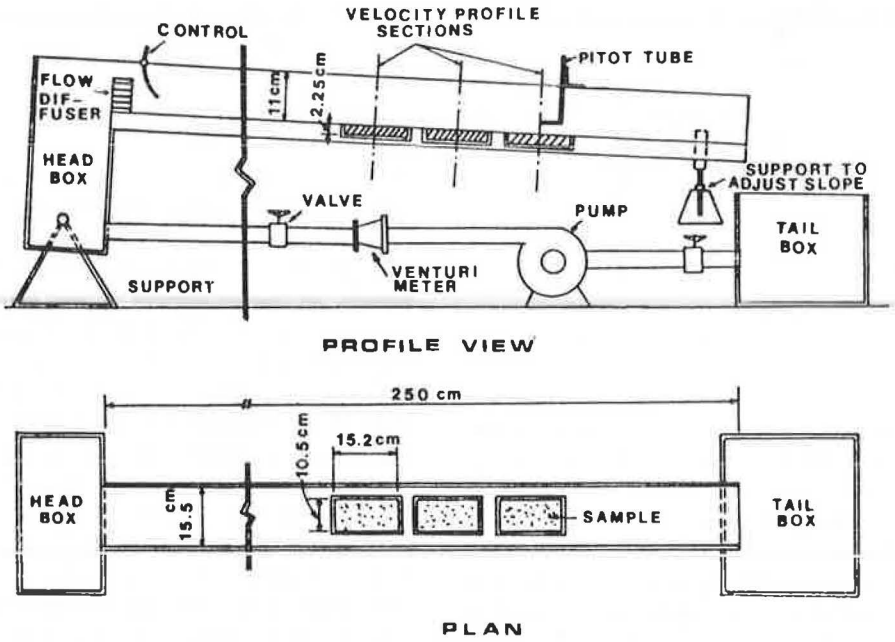

FIGURE 1 Flume and sample containers.

$$V/V_* = 5.5 + 5.75 \log (V_* y/\upsilon) \quad (1)$$

where

V_* = $(\tau/\rho)^{1/2}$ is shear velocity,
V = velocity at depth y in the turbulent region,
ρ = density of water, and
υ = kinematic viscosity of water.

The tractive stresses were determined for five locations across and along the flume and then averaged. The average of tractive stress values obtained by this method was in close agreement with the value of τ obtained using duBoys' equation *(11)*,

$$\tau = \gamma R \sin \alpha \quad (2)$$

where

γ = unit weight of water,
R = hydraulic radius, and
α = angle between the flume and the horizontal surface.

For small flow depth and high slopes where velocity profile measurement was not possible, the tractive stress was estimated by Equation 2.

For each soil sample a total of nine tests were conducted at three flume slopes and three time durations. To reduce the testing time, the flume was designed so that as many as three samples could be tested during the same run. For Ca-montmorillonite samples for which the erosion rate was relatively high, only one sample per run was used. In this case, the rest of the sample locations in the flume were filled with dummy samples made of Plexiglas. For Na-montmorillonite samples for which the erosion rate was relatively low, three samples were placed in the flume for each run. In each test, samples were removed at different time intervals starting with the downstream sample. In initial test runs, all three samples were removed at the same time and tests were conducted for different periods of time. The erosion rates obtained by these two procedures were nearly identical and within the range of measurement errors for each soil sample. The close agreement of erosion rate values of a sample at different time intervals suggests that using three samples in each run did not greatly influence the erosion rate of the samples. The amount of erosion (weight loss) is defined as the difference between the dry weights of the samples before and after testing. The values of weight loss are per unit surface area.

EXPERIMENTAL RESULTS AND DISCUSSION

In addition to erosion tests, the reaction of the clay samples to still water was observed. In this section the reaction of Na-montmorillonite and pure Ca-montmorillonite to still water will be discussed. Then the erosion test results will be presented and discussed.

Behavior of Clays in Still Water

One sample of each pure clay, identical to the samples prepared for the erosion tests, was immersed in water for 10 min and the reaction was recorded. The Na-montmorillonite sample did not show appreciable swell, although dispersion of the surface particles was noticed. The surface of the sample became sticky, as was the case in the erosion tests. The Ca-montmorillonite sample, however, swelled and its thickness increased by about 50 percent. Upward flow of entrapped air in a few locations carried water-laden Ca-montmorillonite upward. The depth of penetration of water into the Na-montmorillonite sample was less than 1 mm; water completely penetrated the Ca-montmorillonite sample.

The behavior of the Ca-montmorillonite in still water is characterized by slaking. Slaking is the breakdown of soil on immersion in water. When an unsaturated soil specimen is immersed in water, the water will penetrate the specimen under the driving force of the matrix and osmotic potential. The air in the voids will be trapped between menisci of the entering water, and air pressure will increase as the water fills the voids. The entrapped air will then exert an enormous pressure causing a rapid increase in void size and disintegration of the soil (*12*, p. 146; *13*, p. 174; *14*, pp. 1–7).

General Observations for Erosion Tests

The mechanism of erosion was observed to vary for the different clay samples tested. The Na-montmorillonite eroded particle by particle. At the beginning of each test the recirculating water was clear and gradually became cloudy indicating the gradual detachment of the clay particles from the sample surface and their suspension in water. The pattern of erosion of the Na-montmorillonite samples was similar to that shown in Figure 2. The three samples shown in this figure represent various erosion times. Except for the dips at the upstream and downstream ends, the sample surface remained flat and smooth after erosion. The form of erosion at the upstream and downstream ends of the samples is believed to be the result of eddies that developed from changes in roughness of the flume bed when the bed changed from the Plexiglas to a soil sample surface. The erosion time of the Na-montmorillonite samples ranged from 30 to 120 min, and the erosion depth varied from 1 to 6 mm. The depth of penetration of water in the samples during the erosion tests was less than 1 mm.

The erosion pattern of the Ca-montmorillonite varied with the chemical additives. No specific erosion pattern was observed for samples of pure Ca-montmorillonite because it had a high erosion rate, two orders of magnitude higher than that of Na-montmorillonite. An erosion pattern of the pure Ca-montmorillonite is shown in Figure 3. Most of the pure Ca-montmorillonite samples eroded in large masses. The samples of the Ca-montmorillonite with 0.80 and 1.60 percent $CaCl_2$ eroded mainly in flaky aggregates; flakes as large as 15 mm were

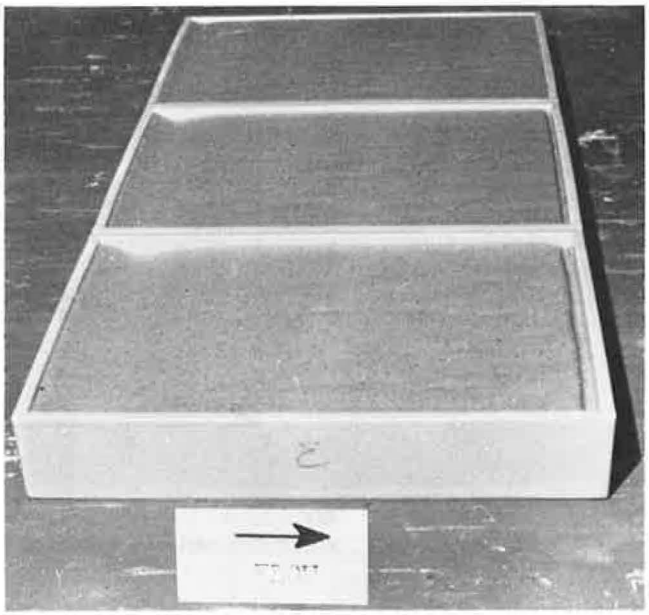

FIGURE 2 Erosion pattern of Na-montmorillonite samples (three different times of erosion increasing from top to bottom).

observed. The Ca-montmorillonite treated with 0.22 percent Na_2CO_3 eroded in soil aggregates. The erosion pattern of the Ca-montmorillonite with 0.88 percent Na_2CO_3 was similar to that of the Na-montmorillonite with an erosion rate on the same order of magnitude as that of the Na-montmorillonite. The erosion time of the pure Ca-montmorillonite samples ranges from 45 sec to 4 min. After the erosion tests were completed, the remaining clays in the sample containers were completely saturated.

Erosion Test Results

A typical relationship between weight loss and erosion time for unsaturated compacted clay samples is shown in Figure 4. Erosion rates for given tractive stresses also are shown in

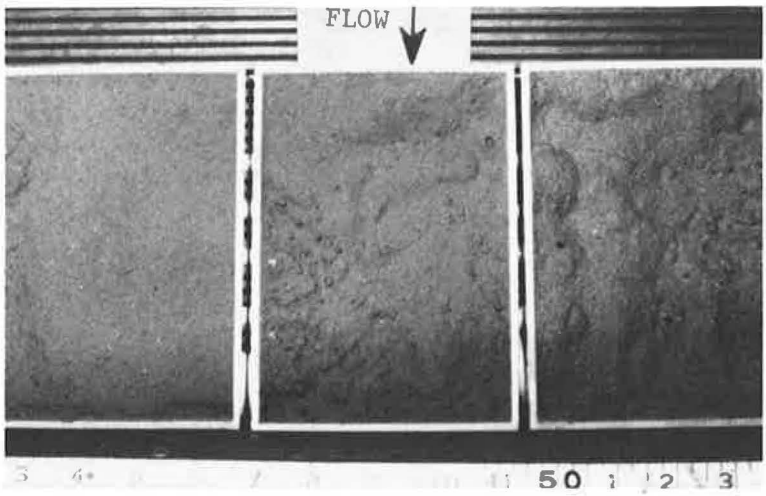

FIGURE 3 Erosion pattern of Ca-montmorillonite (three different times of erosion increasing from left to right).

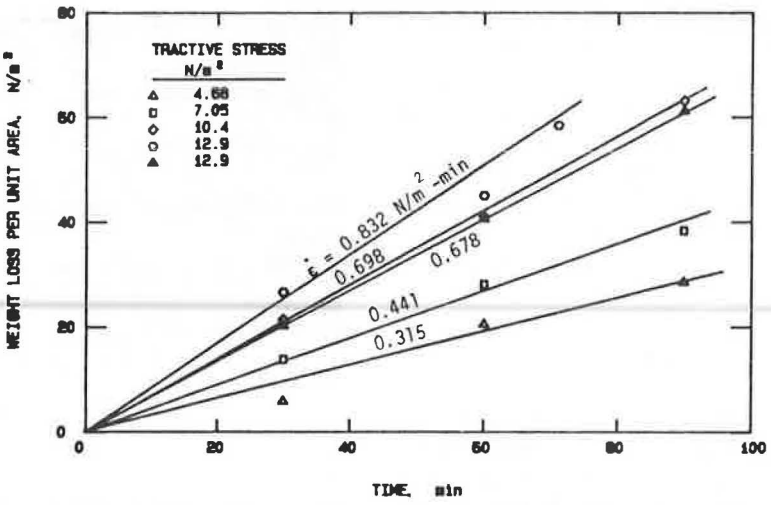

FIGURE 4 Weight loss per unit area versus time for Na-montmorillonite compacted at 34.5 percent water content.

Figure 4. Values of weight losses and erosion rates are per unit surface area. In addition to the tests discussed in this paper, a series of tests was conducted on compacted samples at various water contents and percentages of clay. The test results for all samples are presented elsewhere *(10)*. For most of the samples, weight loss varied linearly with time. The slope of the line relating weight loss to time is defined as the erosion rate. The erosion rate values were determined by using a linear least-squares fit of the data and by imposing the restriction that the lines must pass through the origin as shown in Figure 4.

The erosion rate for Ca-montmorillonite was about two orders of magnitude higher than that for Na-montmorillonite. An erosion rate of 53 N/m^2/min for Ca-montmorillonite versus 0.315 N/m^2/min for Na-montmorillonite under tractive stress of 4.7 Pa was observed. To investigate the cause of such erosional behavior, the Ca-montmorillonite was treated with $CaCl_2$ and Na_2CO_3 and the erosion rates of the treated samples were measured. Calcium chloride was used to increase the TDS and sodium carbonate was used to increase the SAR.

The relationships between erosion rate and tractive stress for the Na-montmorillonite samples and all of the Ca-montmorillonite samples are shown in Figure 5. The relationships between erosion rate and tractive stress may be expressed as

$$\dot{\varepsilon} = C\tau \tag{3}$$

where

$\dot{\varepsilon}$ = erosion rate in N/m^2/min,
τ = tractive stress in N/m^2, and
C = erosion rate coefficient in min^{-1}.

The linear relationships between erosion rates and tractive stresses are determined by a least-squares fit of the data when lines pass through the origin. Values of the erosion rate coefficient (C), TDS, and SAR for the clay samples tested are given in Table 3.

The coefficient (C) for Ca-montmorillonite and Ca-montmorillonite + $CaCl_2$ is 11.8/min, which is 184 times greater than the erosion rate coefficient of 0.064/min for Na-montmorillonite. When Ca-montmorillonite was treated with Na_2CO_3, its erosion rate decreased by two orders of magnitude. The erosion rate of the Ca-montmorillonite + 0.88% Na_2CO_3 samples approached that of the Na-montmorillonite samples (with an erosion rate coefficient of 0.138/min compared with 0.064/min for Na-montmorillonite). The data points shown in Figure 5 for pure Ca-montmorillonite and for Ca-montmorillonite + $CaCl_2$ fall in the same region. These data points are scattered, but they indicate that the addition of $CaCl_2$ had no appreciable influence on the erosion resistance of the Ca-montmorillonite tested.

The relationship between C and SAR is shown in Figure 6. These results indicate that the Ca-montmorillonite samples with SAR = 0.4 were much more erodible than were the Na-montmorillonite samples with SAR = 19.8. When the SAR of the saturation extract was increased, the Ca-montmorillonite became less erodible and its erosion rate decreased by almost two orders of magnitude. Note that the concentration of salts in the saturation extract of Ca-montmorillonite changed slightly when treated with Na_2CO_3, but such a small change will not significantly influence erodibility. Therefore the changes in erosion rate are attributed only to the changes in SAR as shown in Figure 6.

The relationship between the erosion rate coefficient (C) and SAR from Figure 6 may be expressed as

$$C = 4.41\ (\text{SAR})^{-1.34} \tag{4}$$

Here C has units of min^{-1}. The erosion rate ($\dot{\varepsilon}$) can then be estimated for a given tractive stress (t) using Equation 3.

Slaking was the cause of the high erosion rate of the Ca-montmorillonite in this study. Slaking is the breakdown of soil aggregates on immersion in water. Ca-montmorillonite with a low SAR has a flocculated fabric and therefore is highly permeable. As a result, water easily penetrates the clay and slaking

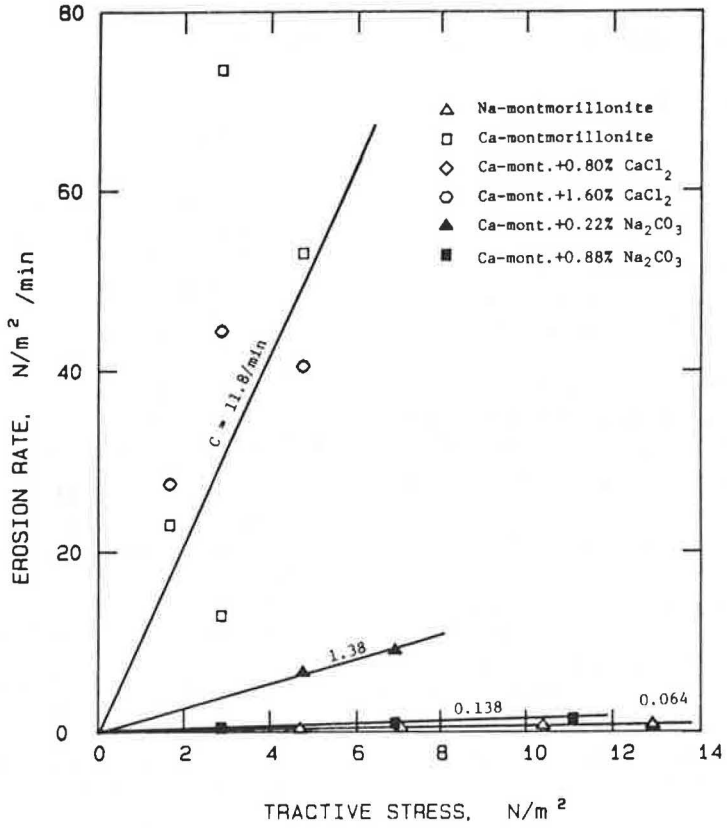

FIGURE 5 Erosion rate versus tractive stress for unsaturated compacted montmorillonite clays.

TABLE 3 CHEMICAL PROPERTIES OF THE SATURATION EXTRACT AND EROSION RATE COEFFICIENT FOR THE CLAY SAMPLES TESTED

Type of Clay	TDS[a] meq/L	SAR[a] $(meq/L)^{1/2}$	Erosion Rate Coefficient C (min^{-1})
Na-montmorillonite	20.5	19.8	0.064
Ca-montmorillonite	7.8	0.4	11.8
Ca-montmorillonite + 0.80% $CaCl_2$	283.0	0.5	11.8
Ca-montmorillonite + 1.60% $CaCl_2$	425.0	0.5	11.8
Ca-montmorillonite + 0.22% Na_2CO_3	8.5	3.9	1.38
Ca-montmorillonite + 0.88% Na_2CO_3	10.7	11.4	0.138

[a]From the saturation extract.

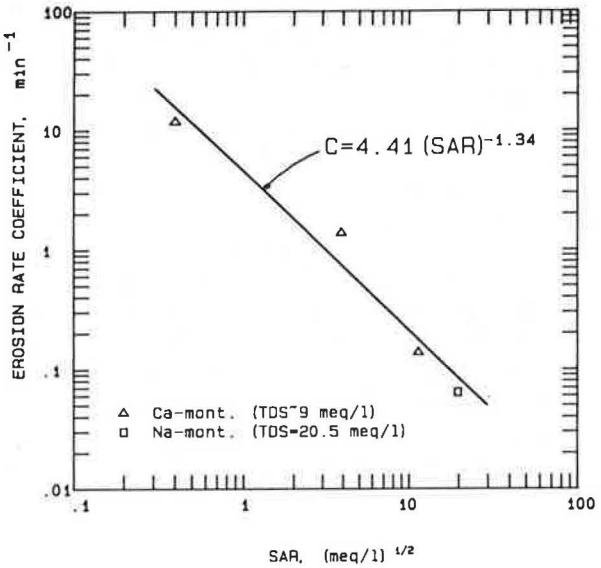

FIGURE 6 Variation of erosion rate coefficient (C) as a function of SAR for unsaturated compacted montmorillonite samples.

occurs. Na-montmorillonite has a dispersed fabric with a low permeability and therefore water cannot easily penetrate the soil. Hence, the soil does not slake and erosion occurs only by detachment and removal of clay particles at the sample surface.

The results of this study were in agreement with those reported by Grissinger *(15)*, who measured the erosion rate of unsaturated compacted soil mixtures containing Na-montmorillonite and Ca-montmorillonite. His results showed that the erosion rate of the soil containing Ca-montmorillonite was about 20 times greater than that of the soil containing Na-montmorillonite. Grissinger used a method of compaction similar to the one used in this study and performed his erosion tests in a flume.

The influence of SAR on the erosion rate of the compacted unsaturated montmorillonite clays was the opposite of results of erosion studies *(2–5, 8, 16)* on saturated consolidated clays. The erodibility of saturated consolidated clays has been found

to increase with increasing SAR (5). The erosion rate of unsaturated compacted clays decreased with increasing SAR.

APPLICATION OF RESULTS IN HIGHWAY ENGINEERING

A concern in highway engineering is erosion damage to highway embankments caused by rainfall and overland flow. Knowledge of the factors that control the erosion resistance of compacted unsaturated soils makes it possible to identify highly erodible soils and develop methods of controlling or reducing the erosion rate of such soils. The results of this study indicate that salt additives (or pore water chemistry) are the controlling factors of erosional behavior of montmorillonite clays. The erosion rate of a highly erodible Ca-montmorillonite can be reduced by two orders of magnitude by treating it with less than 1 percent by weight Na_2CO_3.

Empirical equations (Equations 3 and 4), which can be used to estimate the erosion rate of compacted montmorillonite clays, are developed in this study. From Equation 4 the erosion rate coefficient (C) can be determined for a montmorillonite clay with a known value of SAR. Equation 3 can be used to estimate the erosion rate of the clay as a function of applied tractive stress. Therefore the extent of erosion during a runoff event can be predicted if the applied tractive stresses are assumed and flow duration is known.

CONCLUSIONS

The results of this study have shown that the primary factor influencing the erodibility of unsaturated compacted montmorillonite clays is soil pore water chemistry. The pore water chemistry is characterized by the total dissolved salts (TDS in meq/L) and sodium adsorption ratio (SAR in meq/$L^{1/2}$) of a saturation extract. The erosion rate of the Ca-montmorillonite (with SAR = 0.4 and TDS = 19.8) was two orders of magnitude higher than that of the Na-montmorillonite (with SAR = 19.8 and TDS = 20.5). The erosion rate coefficient (C) (the increase in erosion rate per unit increase of tractive stress) decreased with increasing SAR. C of the Ca-montmorillonite decreased by almost two orders of magnitude, from 11.8 to 0.138/min, when the SAR increased from 0.4 to 11.4. The erosion rate coefficient of the Ca-montmorillonite approached the value of C of the Na-montmorillonite when the SAR of the Ca-montmorillonite approached the SAR of the Na-montmorillonite. The erosion rate of compacted montmorillonite samples may be expressed as a power function of SAR and a linear function of tractive stress.

REFERENCES

1. J. L. Sherard, L. P. Dunnigan, and R. S. Decker. Identification and Nature of Dispersive Soils. *Journal of the Geotechnical Engineering Division*, ASCE, Vol. 102, No. GT4, 1976, pp. 287–301.
2. A. Alizadeh. *Amount and Type of Clay and Pore Fluid Influences on the Critical Shear Stress and Swelling of Cohesive Soils*. Ph.D. dissertation. University of California, Davis, 1974.
3. R. Ariathurai and K. Arulanandan. Erosion Rates of Cohesive Soils. *Journal of the the Hydraulics Division*, ASCE, Vol. 104, No. HY2, 1978, pp. 279–283.
4. K. Arulanandan. Fundamental Aspects of Erosion of Cohesive Soils. *Journal of the Hydraulics Division*, ASCE, Vol. 101, No. HY5, 1975, pp. 635–639.
5. K. Arulanandan, P. Loganathan, and R. Krone. Pore and Eroding Fluid Influences on Surface Erosion of Soil. *Journal of the Geotechnical Engineering Division*, ASCE, Vol. 101, No. GT1, 1975, pp. 51–65.
6. A. Kandiah. *Fundamental Aspects of Surface Erosion of Cohesive Soils*. Ph.D. dissertation, University of California, Davis, 1974.
7. Y. D. Liou. *Hydraulic Erodibility of Two Pure Clay Systems*. Ph.D. dissertation, Colorado State University, Fort Collins, 1970.
8. A. Sargunam, P. Riley, K. Arulanandan, and R. B. Krone. Physicochemical Factors in Erosion of Cohesive Soils. Proc. Paper 9609. *Journal of Hydraulics Division*, ASCE, Vol. 99, No. HY3, March 1973, pp. 555–558.
9. J. L. Sherard and R. S. Decker, eds. *Dispersive Clays, Related Piping, and Erosion in Geotechnical Projects*. ASTM, Philadelphia, Pa., 1977.
10. A. Shaikh. *Surface Erosion of Compacted Clays*. Ph.D. dissertation. Colorado State University, Fort Collins, 1986.
11. V. T. Chow. *Open-Channel Hydraulics*. McGraw-Hill, New York, 1959.
12. K. Terzaghi and R. B. Peck. *Soil Mechanics in Engineering Practice*, 2nd ed. John Wiley & Sons, Inc., New York, 1967.
13. G. G. Sowers. *Introductory Soil Mechanics and Foundations: Geotechnical Engineering*, 4th ed. Macmillan Publishing Co., Inc., New York, 1979.
14. H. F. Winterkorn. Experimental Study of the Attack of Water on Dry Cohesive Soil Systems. In *Special Report 135: Soil Erosion: Causes and Mechanisms; Prevention and Control*. HRB, National Research Council, Washington, D.C., 1973, pp. 1–7.
15. E. G. Grissinger. Resistance of Selected Clay Systems to Erosion by Water. *Water Resources Research*, Vol. 2, No. 1, 1966, pp. 130–138.
16. A. Kandiah and K. Arulanandan. Hydraulic Erosion of Cohesive Soils. In *Transportation Research Record 497*, TRB, National Research Council, Washington, D.C., 1974, pp. 60–68.